

## Research papers

# Magmatic fluid input controlling the geochemical and isotopic characteristics of geothermal waters along the Yadong-Gulu rift, southern Tibetan Plateau



Hui Zhou<sup>a</sup>, Xingxing Kuang<sup>a,b,\*</sup>, Yinlei Hao<sup>a</sup>, Can Wang<sup>a</sup>, Yuqing Feng<sup>a</sup>, Yiguang Zou<sup>a</sup>, Meizhuang Zhu<sup>a</sup>, Chunmiao Zheng<sup>a</sup>

<sup>a</sup> School of Environmental Science and Engineering, Southern University of Science and Technology, Shenzhen 518055, China

<sup>b</sup> Shenzhen Municipal Engineering Lab of Environmental IoT Technologies, Southern University of Science and Technology, Shenzhen 518055, China

## ARTICLE INFO

**Keywords:**  
Geochemistry  
Isotope  
Geothermal energy  
Partial melting  
Tibetan Plateau

## ABSTRACT

Geothermal resources, regarded as sustainable green energy, are attracting increasing attention. The southern Tibetan Plateau possesses the most abundant intermediate-high geothermal resources in China and has enormous potential for geothermal exploration. Geothermal waters from the Yadong-Gulu Rift (YGR), which is considered as the most active geothermal belt of the plateau, are studied based on hydrochemical and isotopic characteristics to understand the spatial variations of fluid origin, evolution, and circulation mechanism as well as heat sources. The hydrochemical characteristics of cold springs and surface waters are consistently characterized by Ca-HCO<sub>3</sub> dominated (Ca-HCO<sub>3</sub> and Ca-HCO<sub>3</sub>-SO<sub>4</sub>) waters while those of geothermal springs present extensive variability with Na-Cl dominated (Na-Cl-HCO<sub>3</sub>, Na-HCO<sub>3</sub>-Cl, Na-Ca-Cl-HCO<sub>3</sub>) and Na-HCO<sub>3</sub> waters. The main geochemical processes controlling the geothermal springs are combinations of silicate weathering, carbonate dissolution, and cation exchange. The characteristics of trace alkali metals and B indicate they undergone common/similar deep process and the potential input of magmatic degassing. The δD and δ<sup>18</sup>O values suggest that cold springs and surface waters are recharged by meteoric water, and geothermal springs are replenished by meteoric water, snow-melt, and magmatic fluid. The mass balance model reveal that dominant carbon sources for geothermal waters can be deeply derived CO<sub>2</sub> (i.e., magmatic source and metamorphic source), contributing from 77% to 99%. Based on empirical chemical geothermometers, Si-Enthalpy mixing model, and geothermometrical modelling, the calculated reservoir temperatures are highly variable (137–312 °C). The circulation depths of geothermal waters are 2.45–6.85 km. A conceptual model is proposed to reveal the deep groundwater circulation.

## 1. Introduction

In response to energy shortage, atmospheric contamination and global warming, geothermal energy which is renewable, low-carbon, and resource-efficient has raising considerable attention (He et al., 2016; Yang et al., 2017; Jolie et al., 2021). Geothermal resources are used worldwide as reliable energy for heat and/or electricity in over 90 countries (Lund and Toth, 2021). China, which accounts for about 8% of the global geothermal sources, has enormous potential for geothermal exploration and exploitation (Kong et al., 2014; Zhang et al., 2019b). The direct utilization of low temperature (<125 °C) geothermal systems in China has been highly developed, whereas electricity generation by intermediate-high temperature (≥125 °C) geothermal systems is still in

the initial stage (Bertani, 2016; Lund and Toth, 2021; Jolie et al., 2021). The Tibetan Plateau, an important part of the Mediterranean-Himalayan geothermal belt, possesses the most abundant intermediate-high temperature geothermal resources in China (Guo, 2012; Guo et al., 2019). Under persistent India-Asia continental collision, the Tibetan Plateau has been strongly uplifted and resulted in a series of approximately N-S trending extensional rifts (Cogan et al., 1998; Yin and Harrison, 2000; Chung et al., 2005). The intermediate-high temperature geothermal systems of the Tibetan Plateau principally distribute along the Indus-Yarlung-Tsangpo suture and extend in N-S direction, strictly controlled by a system of near N-S-trending normal faults and grabens (Hou et al., 2001; Wang et al., 2021). At present, 129 geothermal systems with reservoir temperatures higher than 150 °C and 12 geothermal

\* Corresponding author at: School of Environmental Science and Engineering, Southern University of Science and Technology, Shenzhen 518055, China.  
E-mail address: [kuangxx@sustech.edu.cn](mailto:kuangxx@sustech.edu.cn) (X. Kuang).

systems higher than 200 °C have been found in Tibet (Liao and Zhao, 1999). However, the power generation potential of most geothermal resources has not been evaluated completely.

Economical intermediate-high temperature geothermal systems are commonly due to high geothermal gradients and/or magma chambers at various depths, among which shallow magmatic heat source has the most effective power generation potential (Guo et al., 2009; Jolie et al., 2021). During the 1990s, the Project INDEPTH conducted multiple geophysical surveys in the Yadong-Gulu rift (YGR), the longest rift system of the Tibetan Plateau and one of the most representative N-S trending rifts. Geophysical data revealed the existence of partial melting (granitic magmas) at 15–20 km depth to the north of the YGR (north of the Indus-Yarlung-Tsangpo suture), including (1) strong conventions of P-to-S reflections (Makovskiy et al., 1996); (2) high conductivity zone by magnetotelluric (MT) surveying (Chen et al., 1996); (3) bright spots by seismic reflection profiling (Brown et al., 1996); (4) mid-crustal low-velocity zone through earthquake data (Kind et al., 1996) and (5) pronounced satellite magnetic lows (Alsdorf and Nelson, 1999). The mid-crust partial-melt zone is not limited in the northern of the YGR; it ends at the Indus-Yarlung-Tsangpo suture with a thin conduit and extends ~100 km to the south and upward to the surface in the Kangmar dome (Chen et al., 1996; Unsworth et al., 2005; Xie et al., 2021). It is notable that geothermal surface manifestations are accordance with the underlying partial-melt zone along the YGR (Wei et al., 2001).

Fluid geochemistry can provide significant information for the origin, circulation, evolution, and reservoir temperature of geothermal systems and thus, is critical for the sustainable utilization of geothermal resources (Wrage et al., 2017; Jolie et al., 2021). The Yadong-Gulu geothermal belt, constrained by the YGR, is the most active geothermal belt with the largest geothermal potential of the Tibetan Plateau (Liu et al., 2014; Wang et al., 2018a). Various surface manifestations, including hot springs, boiling springs, geysers, fumaroles, and sinters, occur along the YGR. During the past three decades, geological and geochemical investigations have been extensively conducted as well as systematic studies mainly focused on the genesis of individual geothermal systems including Yangbajing (Zhao et al., 1998; Dor, 2003; Guo et al., 2007; Guo et al., 2010; Yuan et al., 2014; Wang et al., 2022), Yangyi (Guo et al., 2009; Yuan et al., 2014), and Gulu (Zhang et al., 2014) geothermal fields in the northern segment of the rift. The Yangbajing geothermal field was the earliest developed high-temperature geothermal system in China. The installed capacity has reached 26.18 MW and remains active due to the severe energy shortage in Tibet (Zhang et al., 2019b). However, it is not clear whether various geothermal manifestations along the YGR have consistent heat sources and genetic mechanisms.

The major objectives of this study are to (1) investigate the controlling processes of the major solutes and typical trace elements based on the hydrochemical characteristics and geological conditions; (2) determine the recharge sources and carbon sources based on the isotopic characteristics; (3) estimate the equilibrated reservoir temperatures and related circulation depths based on geochemical approaches and geothermometrical modelling and (4) propose a conceptual model for the circulation of the geothermal fluids.

## 2. Study area

The Himalayan-Tibetan orogen, formed by the Cenozoic India-Asia collision, is a collage of Himalayas, Lhasa, Qiangtang, and Songpan-Ganze terranes separated from south to north by Indus-Yarlung-Tsangpo (IYS), Bangong-Nujiang (BNS) and Jinsha (JS) sutures, respectively (Yin and Harrison, 2000; Hou et al., 2015). The continuous India-Asia convergence has resulted in a series near N-S stretching tensile, which rifts from the south of the Himalayas and terminate at the center of the Tibetan Plateau (Cogan et al., 1998; Yin and Harrison, 2000; Chung et al., 2005). These N-S oriented rifts consist of numerous en-echelon arrayed grabens and half grabens, floored by Quaternary

alluvium and/or glacial and widely outcropping Miocene K-rich magmatic rocks (Armijo et al., 1986; Cogan et al., 1998; Guo et al., 2018). The individual graben and half graben valleys are generally a few to about 15 km wide and continuous for tens of kilometers. The high-temperature geothermal resources mostly distribute in both sides of IYS and associated N-S oriented rifts (Hou et al., 2001; Wang et al., 2021). From east to west, there are mainly four hydrothermal belts: comprising Sangri-Cuona, Yadong-Gulu, Shenza-Xietongmen, and Dangreyongco-Dingri (Hou et al., 2001; Wang et al., 2018b).

The YGR is the largest active rift with the most concentrated geothermal resources of the whole Tibetan Plateau which extends 500 km from Yadong (about 27°29'N) to Gulu counties (about 31°10'N) (Armijo et al., 1986; Wang et al., 2018a), as shown in Fig. 1. The YGR cuts through the Lhasa terrane, IYS and Himalayas terrane and can be subdivided into two structurally different segments by the IYS (Wu et al., 2015; Zuo et al., 2021). To the north of the IYS, the northern segment, located in the Lhasa terrane, comprises one graben and three half-grabens including the Geda graben and Angang-Yangyi, Damxung-Yangbajing and Gulu half-grabens (Wu et al., 2011). Between the IYS and Nyainqntanglha range, the faults of YGR symmetrically dip to the east and west, whereas slope to east along Nyainqntanglha (Armijo et al., 1986). The northern segment primarily exposes Paleozoic-Mesozoic metasedimentary lithologies (i.e., phyllite, slate and meta-conglomerate), Carboniferous shallow marine clastic deposits and minor limestone, Cretaceous-Tertiary granitoids (i.e., granite, granodiorite, monzonite granite) of the Gangdese batholith, Paleocene to Eocene volcanic sequences of Linzizong volcanic formation, Miocene K-rich magmatics, and Quaternary sediments (Kidd et al., 1988; Kapp et al., 2005; Liu et al., 2014).

The IYS is the south vergent tight to isoclinal folds, characterized by three rock subunits, from the south to the north: allochthonous turbidites, dismembered ophiolites and associated radiolarites, and turbidites (Burg and Chen, 1984; Hauck et al., 1998). To the south of the IYS, the southern segment of the YGR belongs to the Himalayas terrane and consists of two half-grabens bounded by west-dipping faults including Relong, and Nyeyo grabens (Wu et al., 2011). The southern segment mainly composed by Paleozoic-Mesozoic sedimentary strata of the Tethyan Series with local outcrops of high-grade metamorphic rock (e.g., Kangmar dome) and Neogene granites (Searle et al., 1987; Cogan et al., 1998). The Tethyan Series is a deformed package of predominantly Paleoproterozoic to Eocene metasediments, bounded to the north by the IYS and to the south by the South Tibetan Detachment System (STD) (Burg and Chen, 1984; Burchfiel et al., 1992; Hou et al., 2012). From south to north, the Tethyan Series are composed by Triassic to Cretaceous sequence of principally low-grade metasediments, which varied northward from Cretaceous carbonate platform deposits and marine clastics to Triassic clastic-dominated sediments (Hou et al., 2012). The Kangmar dome crop out along the axis of the North Himalayan anticline, with the Cambrian granitic core mantled by Paleozoic to Jurassic kyanite-grade metasediments which pass upward into low-grade Tethyan sediments (Burg and Chen, 1984; Chen et al., 1990; Hauck et al., 1998).

## 3. Material and methods

Nineteen geothermal springs were collected from eight typical hydrothermal areas along the YGR, including Gulu (GL), Yuela (YL), Ningzhong (NZ), Yangbajing (YBJ), Gariqiong (GRQ), Yangyi (YY), Jiangzi (JZ) and Kangma (KM) (Fig. 1). Additional 12 cold springs and 4 surface waters were collected close to the geothermal springs.

Total dissolved solids (TDS) and pH were measured in-situ with a calibrated portable multi-parameter analyzer (Hanna HI-98194). Temperature was measured with an infrared thermometer (Omegaette OS542). Total alkalinity was determined by a digital titration (Hach 16900 Digital Titrtor) with 1.6N or 0.16N sulfuric acid. Water samples were filtered through 0.45 μm membrane filters and transferred to high-

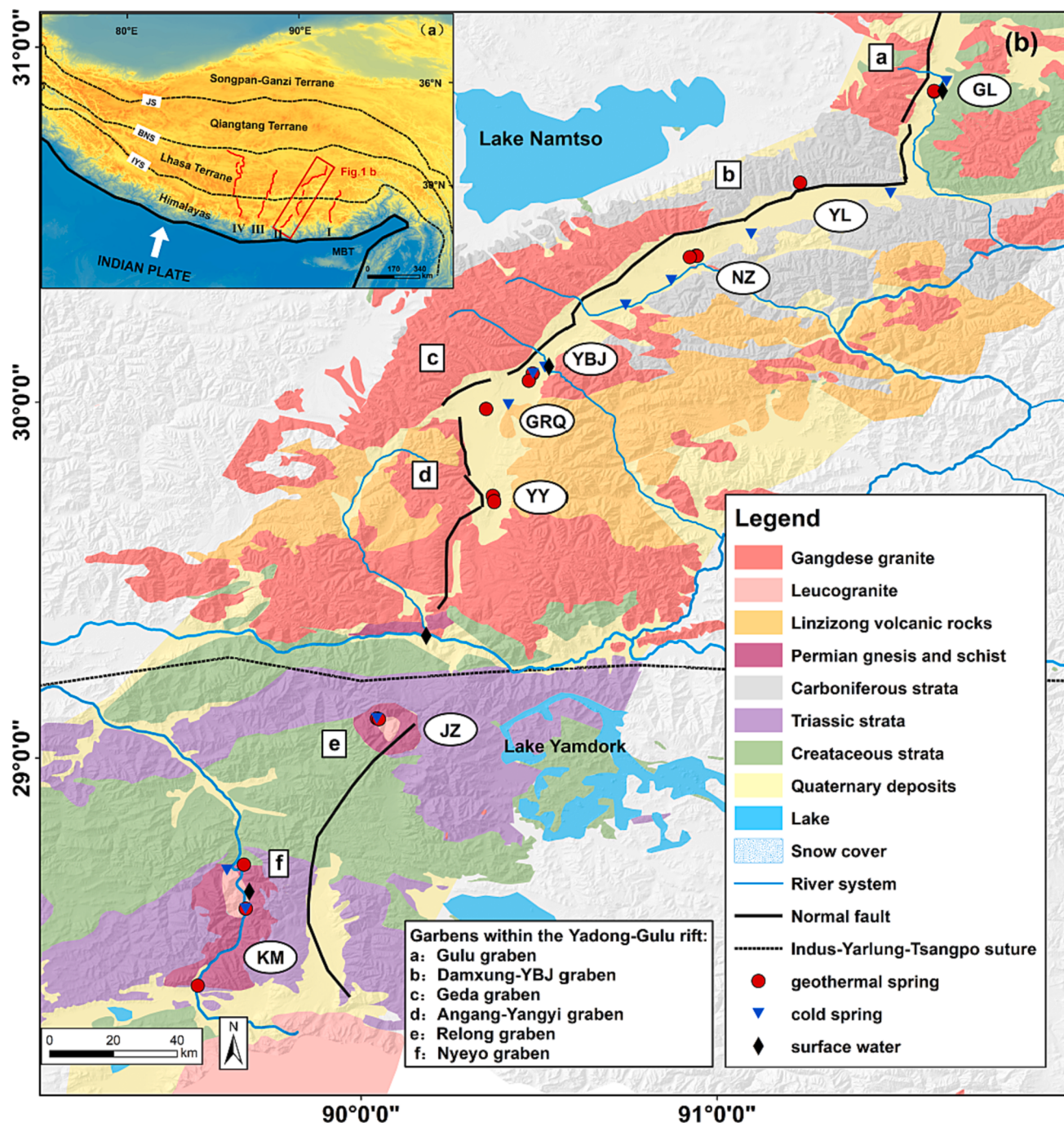


**Fig. 1.** (a) Simplified tectonic map and principle hydrothermal belts of the Himalayan-Tibetan orogen (Yin and Harrison, 2000; Hou et al., 2001; Taylor and Yin, 2009). The principle hydrothermal belts, from east to west, are named: I. Sangri-Cuona hydrothermal belt; II. Yandong-Gulu hydrothermal belt; III. Shenza-Xietongmen hydrothermal belt; IV. Dangreyongco-Dingri hydrthermal belt. Abbreviations: IYS, Indus-Yarlung-Tsangpo suture; BNS, Bangong-Nujiang suture; JS, Jinsha suture; MBT, main boundaries thrust. (b) Generalized geological map, main faults and sampling locations of the Yangdong-Gulu rift (Pan et al., 2004; Taylor and Yin, 2009).

density polyethylene bottles which thoroughly rinsed with filtered waters three times. Samples for silica analysis were diluted by deionized water (1:10) to prevent silica precipitation. Samples for cations and trace elements analysis were acidified to pH < 2 by ultrapure nitric acid. Samples for the oxygen and hydrogen isotope analysis were filled with the container with no headspace and tightly sealed to prevent evaporation. As the samples for the dissolved inorganic carbon isotope analysis, a few drops of HgCl<sub>2</sub> solution were added to prevent bacterial activity. Once collected, all the samples were sealed with parafilm and stored at 4 °C at dark.

In the laboratory, the concentrations of major ions (Cl<sup>-</sup>, SO<sub>4</sub><sup>2-</sup>, K<sup>+</sup>, Na<sup>+</sup>, Ca<sup>2+</sup>, and Mg<sup>2+</sup>) and F<sup>-</sup> were analyzed by ion chromatography (IC, Dionex AQuion). The trace elements (Li, Rb, Cs, and B) were analyzed by inductively coupled plasma mass spectrometry (ICP-MS, Thermo iCAP RQ). Calculated charge balance errors for most samples were within 5% and all the samples were within 10%. Precision of the duplicate analysis at the 95% confidence level was 2% for major and 8% for trace elements. The concentration of SiO<sub>2</sub> was determined by a flow injection analyzer (Lachat QuikChem 8500S2) with the detection limitation of 10 µg/L. The oxygen and hydrogen isotopic composition ( $\delta^{18}\text{O}$  and  $\delta\text{D}$ ) and that

of dissolved inorganic carbon ( $\delta^{13}\text{C}_{\text{TDIC}}$ ) were obtained by isotope ratio mass spectrometer (IRMS, Thermo Scientific 253 Plus). The  $\delta^{18}\text{O}$  and  $\delta\text{D}$  values were reported relative to the Vienna Standard Mean Ocean Water (V-SMOW) with the uncertainties of  $\pm 0.2\text{\textperthousand}$  and  $\pm 0.3\text{\textperthousand}$ , respectively. The  $\delta^{13}\text{C}_{\text{TDIC}}$  values were expressed related to the Vienna Pee Dee Belemnite (V-PDB) with the uncertainties of  $\pm 0.1\text{\textperthousand}$ .

The program PHREEQC (Parkhurst and Appelo, 2013) with

**Table 1**

The physical parameters and chemical compositions of geothermal springs, geothermal well, cold springs and surface waters along the YGR.

Location	Sample ID	Type	T/°C	pH	TDS	Na <sup>+</sup>	K <sup>+</sup>	Ca <sup>2+</sup>	Mg <sup>2+</sup>	Cl <sup>-</sup>	SO <sub>4</sub> <sup>2-</sup>	HCO <sub>3</sub> <sup>-</sup>	CO <sub>3</sub> <sup>2-</sup>	SiO <sub>2</sub>	
mg/L															
The Northern segment															
Guilu															
S01	bsb	83	9.0	2589	944	111	0.26	0.02	859	27	1015	120	151	n.d.	
S02	bsb	84	9.1	2719	1005	122	0.86	1.6	862	16	1086	n.d.	143		
S03 <sup>e</sup>	bsb	86	9.1	3875	1138	130	0.00	0.00	893	235	970	262	147		
S04 <sup>f</sup>	bsb	85	8.0	-	920	111	5.2	1.7	822	10	1424	n.d.	112		
G01	cs	5.5	8.1	124	2.9	0.8	56	3.0	1.1	79	111	n.d.	11		
R01	sw	13	8.3	210	2.9	1.7	47	4.4	0.0	82	95	n.d.	-		
S05	tsb	52	6.9	836	293	48	20	11	90	68	842	n.d.	69		
S06	tsb	50	7.5	958	219	48	80	11	51	26	932	n.d.	71		
S07	tsb	58	7.4	828	284	42	11	8.7	51	26	909	n.d.	72		
S08 <sup>a</sup>	tsb	67	8.0	920	230	46	27	7.8	44	36	764	16	70		
S09 <sup>e</sup>	tsb	69	7.0	1471	240	37	71	15	45	60	856	n.d.	116		
G02	cs	6.4	8.0	135	5.5	1.4	30	8.5	0.02	14	155	n.d.	8.3		
G03	cs	11	8.1	112	4.7	0.86	33	6.9	6.5	23	94	n.d.	-		
Ningzhong	S10	bsb	86	8.6	1747	560	87	11	17	480	232	695	n.d.	134	
S11	bsb	85	8.2	1568	522	82	21	6.4	442	222	634	n.d.	133		
S12	bsb	85	8.0	1748	452	101	7.4	6.2	436	219	653	n.d.	134		
S13 <sup>e</sup>	bsb	88	8.3	2612	637	116	30	7.8	479	362	622	58	128		
S14	bsb	85	8.2	1339	270	39	2.0	0.24	255	34	450	n.d.	147		
S15	bsb	85	7.9	1200	285	27	1.5	0.9	208	47	415	n.d.	152		
G04	cs	9.4	6.4	71	4.8	2.0	15	3.6	1.1	7.1	67	n.d.	23		
G05	cs	6.9	7.5	82	5.7	2.0	18	4.6	1.1	8.6	85	n.d.	22		
Yangbajing	S16 <sup>a</sup>	bsb	84	8.5	1619	405	48	6.9	4.2	469	91	296	32	163	
S17 <sup>a</sup>	bpb	91	7.9	1600	400	46	14	4.2	468	51	439	n.d.	170		
W01 <sup>b,d</sup>	gw	255*	8.4	-	709	135	2.1	0.13	1020	27	363	2.5	582		
G06	cs	9.2	8.2	48	5.1	1.6	16	1.4	1.1	23	43	n.d.	15		
G07	cs	11	8.0	52	4.1	1.1	19	2.0	1.1	10	55	n.d.	22		
R02	sw	4.3	8.3	54	5.5	1.5	19	1.1	1.2	32	37	n.d.	-		
N1 <sup>d</sup>	snw	-	-	-	-	-	-	-	-	-	-	-	-	-	
N2 <sup>d</sup>	snw	-	-	-	-	-	-	-	-	-	-	-	-	-	
Gariqiong	S18	tpb	77	7.6	737	310	23	22	1.1	70	47	632	n.d.	90	
S19	tpb	77	7.4	780	336	20	16	1.5	63	71	632	n.d.	99		
S20 <sup>e</sup>	tsb	80	8.2	1263	274	22	16	2.0	67	39	680	n.d.	106		
S21 <sup>a</sup>	tsb	78	7.6	1140	450	54	14	1.1	66	58	709	n.d.	88		
G08	cs	8.7	7.5	694	65	53	219	26	220	110	282	n.d.	12		
Yangyi	S22	bsb	83	8.6	1133	399	30	15	0.6	181	242	654	n.d.	252	
S23	bsb	83	8.2	1136	425	30	1.4	8.8	166	241	586	n.d.	253		
S24	bsb	85	8.1	1133	436	31	15	0.30	168	221	672	n.d.	253		
S25 <sup>a</sup>	bsb	87	8.5	1708	450	30	1.0	0.00	183	217	357	200	217		
W02 <sup>c</sup>	gw	207*	8.0	1799	490	57	6.5	1.0	183	256	645	29	377		
R03	sw	11	8.4	120	5.9	1.2	26	5.2	3.2	41	79	n.d.	-		
The Southern segment															
Jiangzi	S26	tsb	66	6.6	3502	992	91	81	11	1360	22	1032	n.d.	141	
S27 <sup>a</sup>	tsb	70	7.1	4180	1140	108	82	10	1480	29	1180	n.d.	114		
G09	cs	16	8.2	173	5.7	1.7	41	17	1.1	72	98	n.d.	24		
Kangma	S28	tsb	37	6.1	1648	355	60	38	102	423	8.0	1106	n.d.	61	
S29	tsb	37	6.1	1648	359	57	47	61	381	16	1100	n.d.	246		
S30 <sup>a</sup>	tsb	29	6.6	1770	447	-	149	23	427	18	992	n.d.	45		
S31	tsb	40	6.3	1291	352	54	42	14	375	7	793	n.d.	41		
S32 <sup>a</sup>	tsb	36	7.2	2770	680	69	84	9.4	671	25	1240	n.d.	34		
S33 <sup>a</sup>	tsb	55	7.9	3043	605	155	174	28	964	2.5	987	n.d.	49		
G10	cs	18	6.5	568	7.5	4.9	118	18	1.1	176	220	n.d.	22		
G11	cs	16	8.2	313	6.8	3.7	70	22	1.1	103	159	n.d.	5.0		
G12	cs	4.5	6.5	136	4.7	0.4	39	6.6	1.1	60	73	n.d.	10		
R04	sw	12	8.2	112	2.7	1.8	20	4.4	2.6	20	76	n.d.	-		

Note: bsb = boiling spring with bubbling gas; tsb = thermal spring with bubbling gas; bpb = bubbling pool with bubbling gas; gw = geothermal well; cs = cold spring; sw = surface water; snw = snow water. - = not analyzed; n.d. = below the detected line; <sup>a</sup> = data from Tong et al. (2000); <sup>b</sup> = data from Guo et al. (2007); <sup>c</sup> = data from Guo et al. (2009); <sup>d</sup> = data from Guo et al. (2010); <sup>e</sup> = data from Liu et al. (2014); <sup>f</sup> = data from Wang et al. (2018a). \* = W01 of the YBJ geothermal field with the well depth of 1459 m and maximal temperature of 255 °C; W02 of the YY geothermal field with the well depth of 313 m and maximal temperature of 207 °C. The reservoir lithology for (1) YBJ deep geothermal systems are Himalayan granitic mylonite and fractured granite; (2) YY geothermal systems are Himalayan biotite granite and biotite granite porphyry (Guo et al., 2009).

#### 4. Results

The physico-chemical parameters and chemical compositions, and the isotopic signature of geothermal springs, geothermal wells, cold springs and surface waters are presented in Table 1 and Table 2, respectively. Additional data from previous studies (Tong et al., 2000; Guo et al., 2007, 2009, 2010; Liu et al., 2014; Wang et al., 2018a) are included for comparison.

##### 4.1. Hydrochemical characteristics

Hydrochemical characteristics of the geothermal springs show extensive variability along the YGR, while that for cold springs and

surface waters are relatively uniform. The geothermal springs had outlet temperatures between 29 and 88 °C, TDS values from 737 (fresh water) to 4180 mg/L (brackish/saline water), and the pH from 6.1 to 9.1 (slightly acidic to alkaline). For cold springs and surface waters, the temperatures were in the range of 4.3–18 °C, the TDS values were 48–694 mg/L (fresh water) with similar chemical compositions, and the pH was from 6.4 to 8.4 (neutral to slightly alkaline). The concentrations of the main anions and cations in the geothermal springs were higher than that of the cold springs and surface waters. The anion molarity ( $TZ^- = HCO_3^- + 2CO_3^{2-} + 2SO_4^{2-} + Cl^-$ ) of geothermal springs were in the range of 13.3–61.6 meq/L (average 28.2 meq/L), and the cation molarity ( $TZ^+ = Na^+ + K^+ + 2Ca^{2+} + 2Mg^{2+}$ ) were 12.8–57.3 meq/L (average 27.1 meq/L). The predominant cation for geothermal springs was  $Na^+$ , and the

**Table 2**

Trace elements concentration and isotopic signature of geothermal springs, geothermal well, cold springs and surface waters along the YGR.

Location	Sample ID	Type	F	Li	Rb	Cs	B	$\delta^{2H}$	$\delta^{18O}$
			mg/L					%oV-SMOW	
<b>The Northern segment</b>									
Gulu	S01	bsb	22	21	2.4	4.8	33	-141.6	-15.3
	S02	bsb	13	21	2.5	5.1	35	-136.6	-15.4
	S03	bsb	15	25	-	-	15	-141	-16.1
	S04	bsb	17	16	-	-	26	-149	-19.1
	G01	cs	-	-	-	-	-	-114.8	-15.6
	R01	sw	-	0	n.d	0.30	0.8	-126.8	-17.4
Yuela	S05	tsb	3.0	0.6	0.11	0.18	8.1	-147.5	-19.6
	S06	tsb	2.9	2.2	0.40	0.48	6.9	-149.5	-19.7
	S07	tsb	3.3	2.0	0.41	0.49	6.9	-148.5	-19.3
	S08	tsb	4.0	-	-	-	9.1	-	-
	S09	tsb	2.4	1.6	-	-	6.8	-145	-19
	G02	cs	-	0.01	-	-	-	-131.6	-17.4
Ningzhong	G03	cs	-	-	-	-	-	-129.9	-17
	S10	bsb	5.6	9.2	1.0	2.7	33	-152.9	-19.2
	S11	bsb	8.0	10	1.1	3.4	30	-151.5	-19
	S12	bsb	7.6	12	1.1	3.0	36	-145	-18.5
	S13	bsb	7.5	11	-	-	37	-142	-18.4
	S14	bsb	10	7.6	0.8	3.9	30	-146	-17.6
	S15	bsb	6.7	6.3	0.46	3.0	29	-154.6	-18.6
	G04	cs	-	0.04	0.01	0.01	-	-133.2	-17.8
	G05	cs	-	0.04	0.01	0.01	-	-125.6	-16.7
Yangbajing	S16	bsb	14	13	-	-	55	-	-
	S17	bpb	14	10	1.3	6.5	51	-	-
	W01	gw	18	25	-	-	119	-140.8	-16.6
	G06	cs	-	0.01	0.00	0.00	-	-129.7	-17.8
	G07	cs	-	-	-	-	-	-136.1	-18.5
	R02	sw	-	0.05	0.00	0.20	0.70	-137.1	-18.7
	N1	sw	-	-	-	-	-	-175	-24.5
	N2	sw	-	-	-	-	-	-172	-24.2
Gariqiong	S18	tsb	9.3	2.6	0.28	1.5	10	-153.4	-19.5
	S19	tsb	10	2.1	0.23	1.2	10	-150.9	-16.3
	S20	tsb	9.3	2.4	-	-	11	-145	-18.7
	S21	tsb	12	2.0	0.25	1.0	8.9	-	-
	G08	cs	-	0.20	0.03	0.01	-	-135.8	-17.2
Yangyi	S22	bsb	10	7.4	0.33	1.8	29	-159.2	-19
	S23	bsb	11	7.0	0.32	1.5	33	-152.2	-18.2
	S24	bsb	10	9.1	0.42	1.8	29	-163.1	-19.8
	S25	bsb	24	13	0.50	1.6	38	-	-
	W02	gw	13	11	-	-	46	-	-
	R03	sw	-	0	0.01	0.05	0.06	-145.2	-19.9
<b>The Southern segment</b>									
Jiangzi	S26	tsb	5.3	23	1.8	12	133	-148.5	-15.2
	S27	tsb	5.8	28	2.3	14	146	-	-
	G09	cs	-	0.06	0.00	0.00	-	-	-
Kangma	S28	tsb	0.38	5.6	0.6	1.5	44	-152.5	-16.7
	S29	tsb	1.0	6.2	0.7	1.7	46	-137.3	-14.6
	S30	tsb	2.6	-	-	-	36	-	-
	S31	tsb	3.2	8.3	2.6	3.0	20	-155.8	-17.3
	S32	tsb	6.5	13	0.9	6.5	138	-	-
	S33	tsb	2.1	24	5.2	22	125	-	-
	G10	cs	-	0.6	0.02	0.09	0.20	146.5	-20
	G11	cs	-	0.05	0.00	0.00	0.09	-145.2	-19.1
	G12	cs	-	0.04	0.01	0.00	0.07	-127.2	-17.7
	R04	sw	-	0.03	0.00	0.00	0.07	-95	-12.9

predominant anions were  $\text{Cl}^-$  and/or  $\text{HCO}_3^-$ . For cold springs and surface waters, the anion molarity ( $\text{TZ}^-$ ) were 1.1–13.1 meq/L (average 3.3 meq/L), and the cation molarity ( $\text{TZ}^+$ ) were 1.2–17.3 meq/L (average 3.6 meq/L). The predominant cation for cold springs and surface waters was  $\text{Ca}^{2+}$ , and the predominant anion were  $\text{HCO}_3^-$  and/or  $\text{SO}_4^{2-}$ .

#### 4.2. Diagnostic trace elements

Diagnostic trace elements, represented by Li, Rb, Cs, B, and  $\text{F}^-$  are regarded as a typical geothermal suite (Li et al., 2021; Yi et al., 2021). The concentrations of Li, Rb, Cs, and B in the cold springs and surface waters ranged from 5.6 to 641  $\mu\text{g}/\text{L}$ , 0.01 to 25  $\mu\text{g}/\text{L}$ , 1.92 to 300  $\mu\text{g}/\text{L}$ , and 65 to 800  $\mu\text{g}/\text{L}$ , respectively (Table 2), and those from geothermal springs discharged at a broad range: 0.6–28 mg/L, 0.11–5.2 mg/L, 0.18–22 mg/L and 6.8–146 mg/L, respectively. Concentrations of  $\text{F}^-$  in the geothermal waters were in the range of 0.38–24 mg/L.

#### 4.3. Stable isotopic composition

The  $\delta^{18}\text{O}$  values of surface waters, cold springs, and geothermal springs varied from -19.9 to -12.9‰ (with an average of -17.3‰), -20.0 to -15.6‰ (with an average of -17.7‰), and -19.9 to -14.6‰ (with an average of -17.9‰), respectively. The  $\delta\text{D}$  values of surface waters, cold springs, and geothermal springs ranged from -145.2 to -95.0‰ (with an average of -126.0‰), -146.6 to -114.8‰ (with an average of -132.3‰), and -163.1 to -136.6‰ (with an average of -148.9‰), respectively. The  $\delta^{13}\text{C}_{\text{TDIC}}$  values of the geothermal springs range from -4.68‰ to 0.24‰ with an average of -2.40‰.

#### 4.4. Spatial variations of geochemistry

The hydrochemical facies of geothermal springs, geothermal well, cold springs, and surface waters are visualized in the Piper diagram (Fig. 2) (Piper, 1944). The hydrochemical facies of cold springs and surface waters in the YGR are:  $\text{Ca}-\text{HCO}_3$  and  $\text{Ca}-\text{HCO}_3-\text{SO}_4$  whereas

those of geothermal waters are more available:  $\text{Na}-\text{Cl}$ ,  $\text{Na}-\text{Cl}-\text{HCO}_3$ ,  $\text{Na}-\text{HCO}_3-\text{Cl}$ ,  $\text{Na}-\text{HCO}_3$ ,  $\text{Na}-\text{Ca}-\text{HCO}_3-\text{Cl}$ , and  $\text{Na}-\text{Ca}-\text{Cl}-\text{HCO}_3$ .

Based on the geographical location, hydrochemical types, and trace elements, the geothermal springs can be distinguished as three groups (Fig. 3):

- Group 1 (Na-Cl dominated waters): this group includes  $\text{Na}-\text{Cl}-\text{HCO}_3$ ,  $\text{Na}-\text{HCO}_3-\text{Cl}$  types found in the GL, NZ, YBJ, and YY geothermal fields of the northern segment.
- Group 2 (Na-HCO<sub>3</sub> dominated waters): this group includes Na-HCO<sub>3</sub> type related to the YL and GRQ geothermal fields of the northern segment.
- Group 3 (Na-Cl dominated waters): this group includes  $\text{Na}-\text{Ca}-\text{Cl}-\text{HCO}_3$ ,  $\text{Na}-\text{Cl}-\text{HCO}_3$  and  $\text{Na}-\text{HCO}_3-\text{Cl}$  types in the JZ and KM geothermal fields of the southern segment.

## 5. Discussion

### 5.1. Processes controlling major solute

The common solutes of the deep reservoir fluids can be conveniently classified into two groups: (a) conservative components (e.g.,  $\text{Cl}^-$ ) which display conservative behavior of water-rock interaction; and (b) reactive components (e.g.,  $\text{Na}^+$ ,  $\text{K}^+$ ,  $\text{Ca}^{2+}$ ,  $\text{Mg}^{2+}$ ) which are controlled by the temperature-dependent water-rock interactions (Nicholson, 1993; Arnarsson, 2000). Therefore, molar (or equivalent) ratios of major solutes have been widely applied to provide insight into the governing geochemical processes (e.g., Yang et al., 2019; Wu et al., 2021; Lee et al., 2021).

The hydro-geological setting of the study region is complex, being characterized by volcanic, metamorphic and sedimentary environments. The dominant anion of geothermal waters shows a geographical variation in  $\text{Cl}^-$  and  $\text{HCO}_3^-$ , while the dominant cation is distinctly  $\text{Na}^+$  (Fig. 2). The concentration of  $\text{Na}^+$  in geothermal springs are well correlated with  $\text{Cl}^-$  ( $r = 0.90$ ) with the enrichment of  $\text{Cl}^-$  (up to 40 meq/

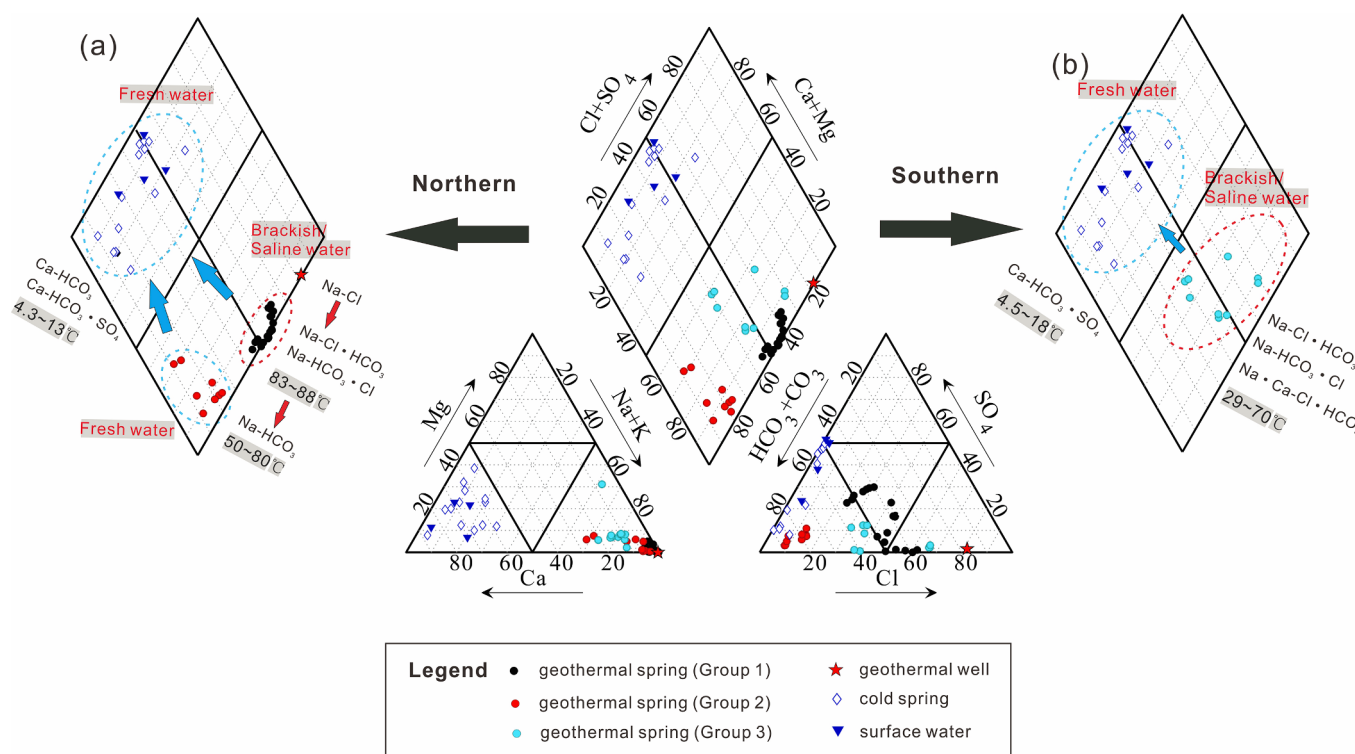


**Fig. 2.** Piper diagram for the investigated geothermal springs, geothermal wells, cold springs, and surface waters along the YGR, and corresponding detailed conditions of (a)the northern segment (north of the IYS), and (b) the southern segment (south of the IYS).

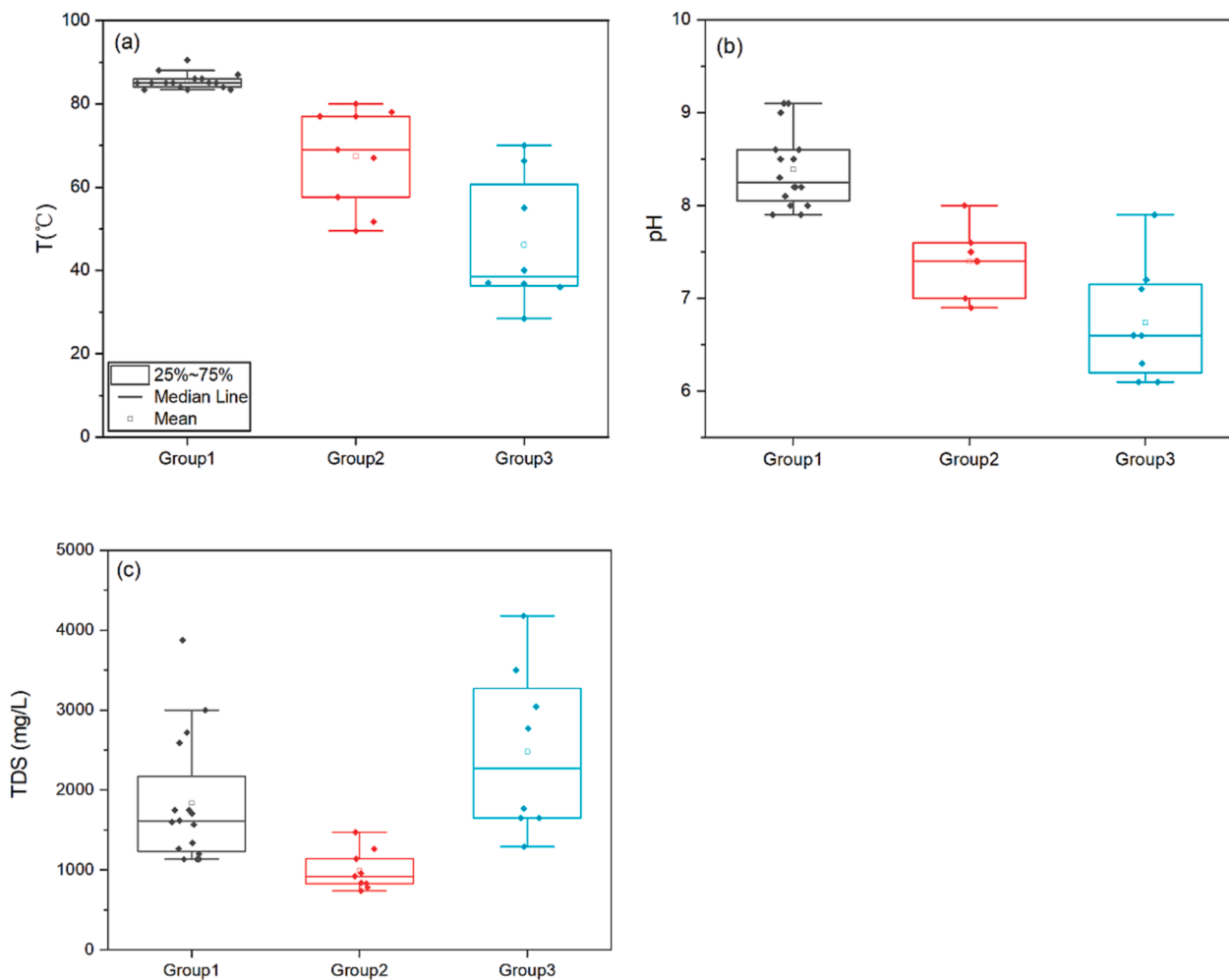
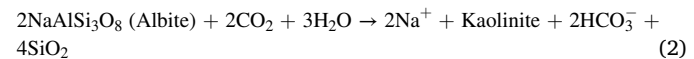


**Fig. 3.** Box and whisker plots of (a) Temperature, (b) pH and (c) TDS values of geothermal waters from different groups.

L), suggesting the potential influence of geothermal fluids or halite dissolution. The deviation of  $\text{Na}^+/\text{Cl}^-$  molar ratio from the 1:1 line (Fig. 4a), the undersaturated of halite (Table 5) and the rarely distribution of evaporite unit, manifesting that halite dissolution (Eq. (1)) are not the dominated source of  $\text{Na}^+$  and  $\text{Cl}^-$  (Fontes and Matray, 1993; Yang et al., 2019). Given that the widely distributed of the granite (Gangdese granite and Leucogranite) and volcanic rocks, the enrichment of  $\text{Na}^+$  in the geothermal springs are possible deriving by the leaching of silicate minerals (e.g., incongruent dissolution of Albite; Eq. (2)), which can additionally increase the alkalinity. The  $(\text{Ca}^{2+}+\text{Mg}^{2+})$  vs.  $(\text{HCO}_3^-+\text{SO}_4^{2-})$  diagram (Fig. 4b) shows that all the geothermal springs locate above the 1:1 line, which support the hypothesis of the occurrence of silicate weathering (e.g., Negri et al., 2018; Fan et al., 2019; Yang et al., 2019). To define the dissolution of silicate minerals, the thermodynamic activity plots are applied in the  $\text{Na}_2\text{O}-\text{Al}_2\text{O}_3-\text{SiO}_2-\text{H}_2\text{O}$  and the  $\text{K}_2\text{O}-\text{Al}_2\text{O}_3-\text{SiO}_2-\text{H}_2\text{O}$  systems (Freeze and Cherry, 1979; Guler and Thyne, 2004; Raychowdhury et al., 2014). Most geothermal springs fall around the triple point junction of albite (K-feldspar), paragonite (muscovite) and kaolinite, suggesting that the  $\text{Na}^+$  and  $\text{K}^+$  are controlled by the above minerals (Figs. 5a and b). The SI of gypsum of all the samples are undersaturated (Table 5) and the trend of gypsum dissolution (Eq. (3)) is not obvious, which suggest the limit contribution of gypsum dissolution (Fig. 4d). The cold springs and surface waters are dominated by the dissolution of carbonate (calcite/aragonite and dolomite; Eqs. (4) and (5)) as shown in Figs. 4b and d.



The reaction of cation exchange can be generalized as Eq. (6) and the influence of cation exchange can be calculated by the relationship of corrected bivalent cation and corrected  $\text{Na}^+$  (Negri et al., 2018; Hosono and Yamanaka, 2021). The  $(\text{Na}^++\text{K}^+-\text{Cl}^-)/[(\text{Ca}^{2+}+\text{Mg}^{2+})-(\text{HCO}_3^-+\text{SO}_4^{2-})]$  equivalent ratio of geothermal springs are close to 1:1 trend line (Fig. 4c), suggesting that the exchange of major cations is one of the dominating processes (Jankowski et al., 1998; Yang et al., 2019). The cold springs and surface waters cluster close to the origin, indicating that the cation exchange has little influence on the chemistry (Verma et al., 2016). Compared to the cold springs, the geothermal waters are enriched in  $\text{Na}^+$  and  $\text{Cl}^-$ , showing a deep and long-term circulation path (e.g., Zhang et al., 2019a).



The  $\text{Na}-\text{HCO}_3$  waters in the geothermal systems are commonly associated with the  $\text{CO}_2$  dissolution at the depth and can be generally formed by two processes (Sracek and Hirata, 2002; Dupalova et al., 2012; Sracek et al., 2019): (a) carbonate dissolution combined with

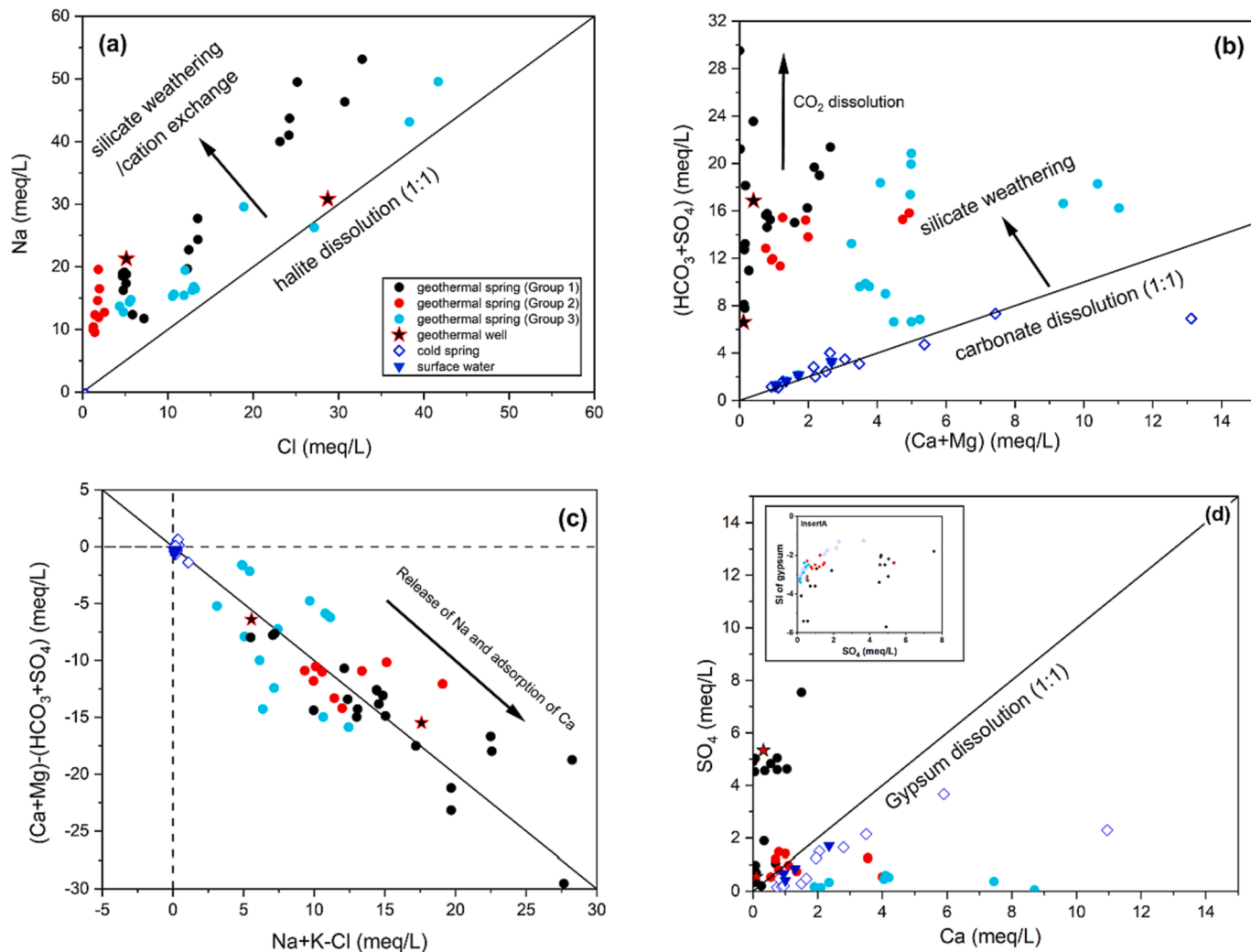
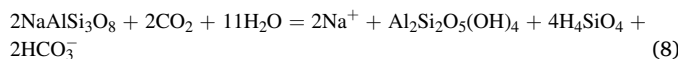
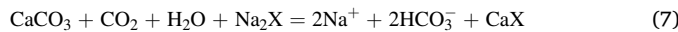


**Fig. 4.** Ionic ratios of (a) Cl vs. Na; (b) (Ca+Mg) vs. (HCO<sub>3</sub>+SO<sub>4</sub>); (c) (Na+K-Cl) vs. [(Ca+Mg) - (HCO<sub>3</sub>+SO<sub>4</sub>)]; and (d) Ca vs. SO<sub>4</sub> (InsertA: SO<sub>4</sub> vs. SI of gypsum) of the geothermal springs, geothermal wells, cold springs, and surface waters along the YGR.

cation exchange expressed as Eqs. (7), and (b) reaction between silicates and CO<sub>2</sub> expressed as Eq. (8).



All the geothermal waters are oversaturated with CO<sub>2</sub> relative to the atmosphere, where P<sub>CO<sub>2</sub></sub> in the range of 10<sup>-2.90</sup> to 10<sup>-0.03</sup>, up to several orders of magnitude higher than the saturation of atmospheric CO<sub>2</sub> (P<sub>CO<sub>2</sub></sub> = 10<sup>-3.40</sup>). Meanwhile, CO<sub>2</sub> is the dominating compound of bubbling gases in the YGR (e.g., Zhang et al., 2017; Klemperer et al., 2022) and thus CO<sub>2</sub> can be a significant factor controlling water-rock interactions. The SIs show that geothermal springs are generally close to saturation with respect to carbonate phases (calcite, aragonite and dolomite) (Table 5), which confirms that the precipitation of these mineral phases should have occurred. Fig. 4b shows the significantly enrichment of HCO<sub>3</sub><sup>-</sup> which can be also attributed to CO<sub>2</sub>-induced silicate hydrolysis. This suggests that both processes possibly operate simultaneously and the CO<sub>2</sub> dissolution increases mineral dissolution and enhances weathering processes (Dupalova et al., 2012; Kis et al., 2020).

The depleted Ca<sup>2+</sup> in the geothermal springs can also be attributed to the cation exchange and CO<sub>2</sub> dissolution (Guo et al., 2009; Lambrakis et al., 2013). The cation exchange processes (Eq. (6)) lead to the

continuous removal of Ca<sup>2+</sup> as shown in Fig. 4c. For geothermal fluid ascend from depth, the decrease of external pressure causes CO<sub>2</sub> degassing and in turn induces HCO<sub>3</sub><sup>-</sup> transformed to CO<sub>3</sub><sup>2-</sup> as expressed by the Eq. (9). With the increasing of CO<sub>3</sub><sup>2-</sup> concentration, the Ca-carbonate precipitation which reduce the Ca<sup>2+</sup> concentration occurred (Eq. (10)). Concentrations of Ca<sup>2+</sup> were negative correlation with F<sup>-</sup>. Most of the geothermal waters are undersaturated for fluorite and oversaturated for calcite (Table 5). This suggests that the decrease of Ca<sup>2+</sup> would promote the release of F-bearing minerals which are commonly prevail in granitic terrains.



## 5.2. Processes controlling typical trace elements

Typical trace elements (Li, Rb, Cs and B), regarded as conservative constituents, are insensitive to the dilution or boiling processes and therefore useful for providing information on the source of deep geothermal fluid (Giggenbach et al., 1994; Pasvanoglu, 2020; Shoedarto et al., 2020). These typical trace elements are also enriched in the fluid associate with the end step of crystallization of the granitic magma (Grimaud et al., 1985).

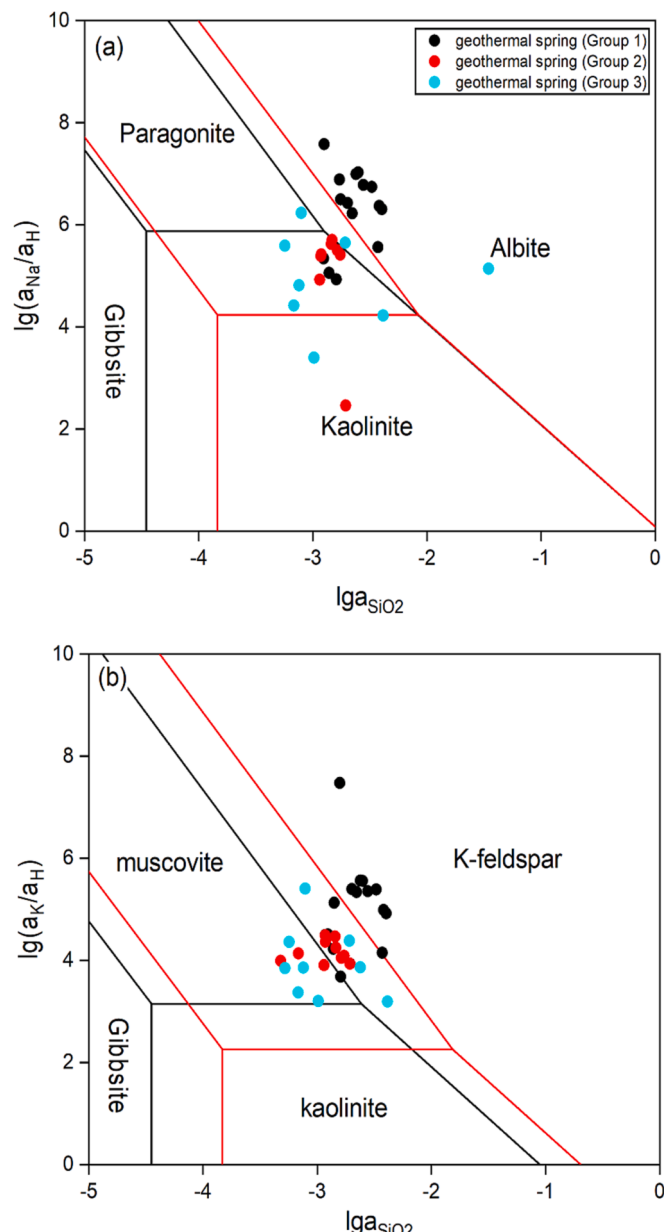


**Fig. 5.** Stability fields of (a)  $\text{Na}_2\text{O}-\text{Al}_2\text{O}_3-\text{SiO}_2-\text{H}_2\text{O}$  system; and (b)  $\text{K}_2\text{O}-\text{Al}_2\text{O}_3-\text{SiO}_2-\text{H}_2\text{O}$  system relative to geothermal springs of the YGR. The phase boundaries are plotted for 100 °C (in black) and 200 °C (in red) based on the thermodynamic data.

Despite concentration of the trace alkalies for geothermal springs varies greatly, the good correlations between the trace alkalies and  $\text{Cl}^-$  ( $r > 0.83$ ), indicate that they originate from the deep reservoir. Figs. 6a – c shows the relations between the trace alkali metals (Li, Rb, and Cs) and B relative to the median rock ratios, and all three alkali metals are less mobile than B. The depletion in the trace alkali metals can be attributed to: (1) the uptake of the trace alkali metals (Li, Rb, and Cs) into major alkali metals (Na and K); (2) the addition of B by magmatic degassing (Kaasalainen and Stefansson, 2012; Wrage et al., 2017).

In the geothermal systems, the three trace alkali metals were acquired by the fluids in the early formation stages, once added to the fluids they were remain basically unchanged, and not formed their own secondary minerals (Goguel, 1983; Giggenbach and Soto, 1992; Kaasalainen and Stefansson, 2012). However, these trace alkali metals can also be taken up into some geothermal alteration minerals such as quartz, chlorite, illite, clays, and zeolites (Giggenbach et al., 1994;

Kaasalainen and Stefansson, 2012). Relative concentrations of Li, Rb, and Cs for the geothermal springs are plotted on the Li-Rb-Cs ternary diagram to identify the existence of the common origin and deep processes (Fig. 7a). All the geothermal springs are far away from the isochemical dissolution of average crustal rock (remarked “rock”), pointing toward the removal of Rb with secondary layer silicates (i.e., illite which removes the initial Rb in the process of crystallization) under elevated temperatures ( $>300$  °C) (Giggenbach et al., 1994; Shoedarto et al., 2020). For Li, which survived in the early stages of water-rock interaction under high temperature, commonly had the possibility to be incorporated into the secondary quartz during the cooling process of all the geothermal springs (Giggenbach and Soto, 1992). However, the good relationship between Li and Cl suggests the limited Li-depletion (Arnorsson, 2000). The Li/Cs ratios, generally dependent on the lithology (around 1 for granite), range from 1.1–5.0 for the geothermal springs (Giggenbach and Soto, 1992; Pasvanoglu, 2020). The deep melting fluid (Li-depletion) can provide potential contribution to geothermal fluids (Ni et al., 2017). The geothermal springs plot close to each other and this suggests that they originate from similar reservoir or under similar processes.

Relative concentrations of Cl, Li, and B, which have varying degrees of conservative behavior, are plotted on the Cl-Li-B ternary diagram (Fig. 7b) to trace the deep source of the fluids (Giggenbach and Soto, 1992). Due to the incompatible behavior of B and Cl at high temperature (especially higher than 150 °C), the Cl/B ratios can record the rock type during the deep circulation process and have been regarded as suitable geochemical indicator to identify the input of magmatic vapor (Giggenbach, 1995; Arnorsson and Andrsdttir, 1995; Bernard et al., 2011, Reyes and Trompetter, 2012). As the water-rock interaction processes proceed, the initial aqueous Cl/B ratio changes as B concentration is added by rock dissolution, while the supplement of  $\text{Cl}^-$  concentration is limited and thus gradually approach to the wall rock (Arnorsson, 1995; Dotsika, 2015). Geothermal waters with low Cl/B molar ratio contain abnormally high B (up to 137.5 mg/L), which is higher than the average crustal abundances (10–40 mg/L), and possibly attributed to the supply of B from the magmatic vapor of degassing magma (Goguel, 1983; Arnorsson, 1995; Dotsika, 2012). The Cl/B molar ratios of geothermal waters (in the range of 1.49–9.74) are significantly lower than the seawater (=1313), indicating that there is no contribution by formation waters (Yuan et al., 2014). The good correlation between B and Cl ( $r = 0.83$ ) also indicates the occurrence of mixing processes with cold waters during the ascending process (Arnorsson, 2000).

### 5.3. Recharge sources and carbon sources of geothermal water

#### 5.3.1. Recharge sources

Various sources can affect the composition of geothermal waters, such as deep-circulating meteoric waters, magmatic waters, formation and metamorphic waters (Nicholson 1993). Stable hydrogen and oxygen isotopes are powerful tools to determine the recharge sources and water-rock interactions of the geothermal system (e.g., Yang et al., 2017; Qiu et al., 2018; Sracek et al., 2019). As shown in Fig. 8, all the surface waters and cold springs are generally parallel to the global meteoric water line (GMWL) defined by Craig (1961), indicating they are originated from local meteoric with no or poor evapo-concentration. Most geothermal springs distribute close to the GMWL which also indicate their meteoric origin. Compared with the surface waters and cold springs nearby, geothermal springs present significant enrichment in  $\delta^{18}\text{O}$  (geothermal shift: Craig, 1963), which can be attributed to high-temperature water-rock interactions (Craig, 1963; Clark and Fritz, 1997; Arnorsson, 2000). However, water-rock interactions normally limit  $\delta\text{D}$ -shift since little hydrogen occurs in most rocks relative to that in the fluids (Giggenbach, 1992; Nicholson, 1993). The incongruent dissolution of Na-feldspars (Eq. (2)) and the mixing processes discussed above would also theoretically counteract the observed  $\delta\text{D}$ -shift (Giggenbach, 1992; Hensen et al., 2007). Thus, the non-horizontal isotopic

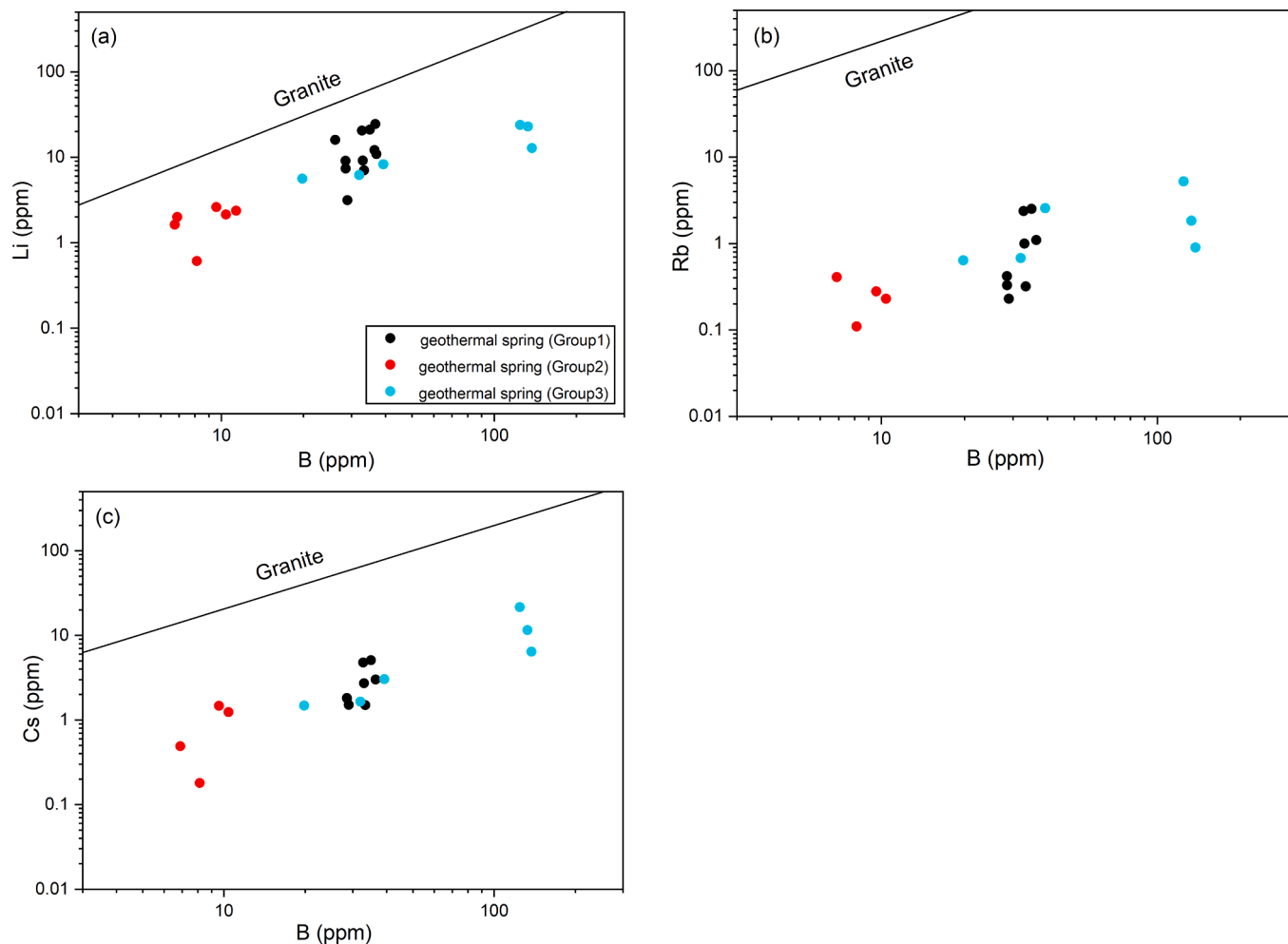


**Fig. 6.** Relationship between (a) B vs. Li; (b) B vs. Rb; (c) B vs. Cs for geothermal springs of the YGR. The solid line is the median rock ratios of granite (Huang et al., 2010; Fan et al., 2021).

trends of geothermal springs possibly suggest the input of magmatic fluids. As shown in Fig. 8, the feeding source of the geothermal waters falls into the mixing area of three end members, including meteoric water, snow-melt, and magmatic fluid.

The mixing ratio of magmatic water can be estimated, as follows (Giggenbach, 1992):

$$\alpha = (\delta_{\text{GW}} - \delta_{\text{SW}})/(\delta_{\text{MW}} - \delta_{\text{SW}}) \quad (11)$$

where  $\alpha$  is the mixed percentage of magmatic water;  $\delta_{\text{GW}}$ ,  $\delta_{\text{MW}}$  and  $\delta_{\text{SW}}$  is the  $\delta D$  (‰ V-SMOW) compositions of geothermal, magmatic, and snow waters, respectively. The contribution of the magmatic waters for geothermal springs in the Group 1, Group 2 and Group 3 are in the range of 15–31%, 14–16%, and 21–28%, respectively. This suggests that Group 2 is less affected by magmatic fluids with respect to Group 1 and Group 3 likely due to a shallow circulation depth.

Given the negative correlation between heavy hydrogen and oxygen isotope composition and elevation (altitude effect), the recharge elevation can be estimated by the equation established by Yu et al. (1984):

$$H_{\text{RE}} = -(\delta D_{\text{RE}} + 30.2)/0.026 \quad (12)$$

where  $H_{\text{RE}}$  represents the recharge elevation (m),  $\delta D_{\text{RE}}$  is the  $\delta D$  value of the intersection point A ( $\delta D = -163.2$ ) and B ( $\delta D = -182.6$ ). The average recharge elevations of the geothermal waters for the northern and the southern segments are 5116 m and 5862 m, respectively. Based on the regional geological condition, the Nyechen Tanglha mountains (about 5500–6000 m) in the northeast and the Himalayan mountains in the

south (about 6000 m) can be the main recharge area of the geothermal springs. The snow-melt water is prone to infiltrate the YGR, and circulate deeply.

### 5.3.2. Carbon sources

Four potential sources can be responsible for the dissolved carbon in the geothermal waters: atmospheric carbon dissolved by rainwater ( $C_{\text{atm}}$ ), organic carbon in the sedimentary strata or soil zone ( $C_{\text{org}}$ ), carbon derived from carbonate mineral dissolution ( $C_{\text{carb}}$ ), deeply derived  $\text{CO}_2$  ( $C_{\text{deep}}$ ) including magmatic source and metamorphic  $\text{CO}_2$  (Chiodini et al., 2000; Karlstrom et al., 2013; Chiodini et al., 2020). The atmospheric  $\text{CO}_2$  have an average  $\delta^{13}\text{C}_{\text{atm}}$  value of -8‰ with low partial pressure ( $P_{\text{CO}_2} = 0.0003\text{bar}$ ) and has thus negligible contribution to geothermal waters (Graven et al., 2017; Karakus et al., 2019).

The multiple carbon sources contributing to  $T_{\text{DIC}}$  (total dissolved inorganic carbon) can be identified by the carbon mass balance model, as follows (Chiodini et al., 2000):

$$C_{\text{exter}} = T_{\text{DIC}} - C_{\text{carb}} \quad (13)$$

$$\delta^{13}\text{C}_{\text{exter}} \times C_{\text{exter}} = \delta^{13}\text{C}_{\text{TDIC}} \times T_{\text{DIC}} - \delta^{13}\text{C}_{\text{carb}} \times C_{\text{carb}} \quad (14)$$

where  $C_{\text{carb}}$  and  $\delta^{13}\text{C}_{\text{carb}}$  represent the carbon from the carbonate dissolution (mol/L) and related isotopic composition (‰), respectively;  $C_{\text{exter}}$  and  $\delta^{13}\text{C}_{\text{exter}}$  represent the carbon from external sources (mol/L) and related isotopic composition (‰), respectively. The  $C_{\text{carb}}$  can be calculated by the equilibrium of Ca/Mg carbonate dissolution and gypsum/anhydrite dissolution ( $C_{\text{carb}} = \text{Ca} + \text{Mg} - \text{SO}_4$  in mol/L). For the

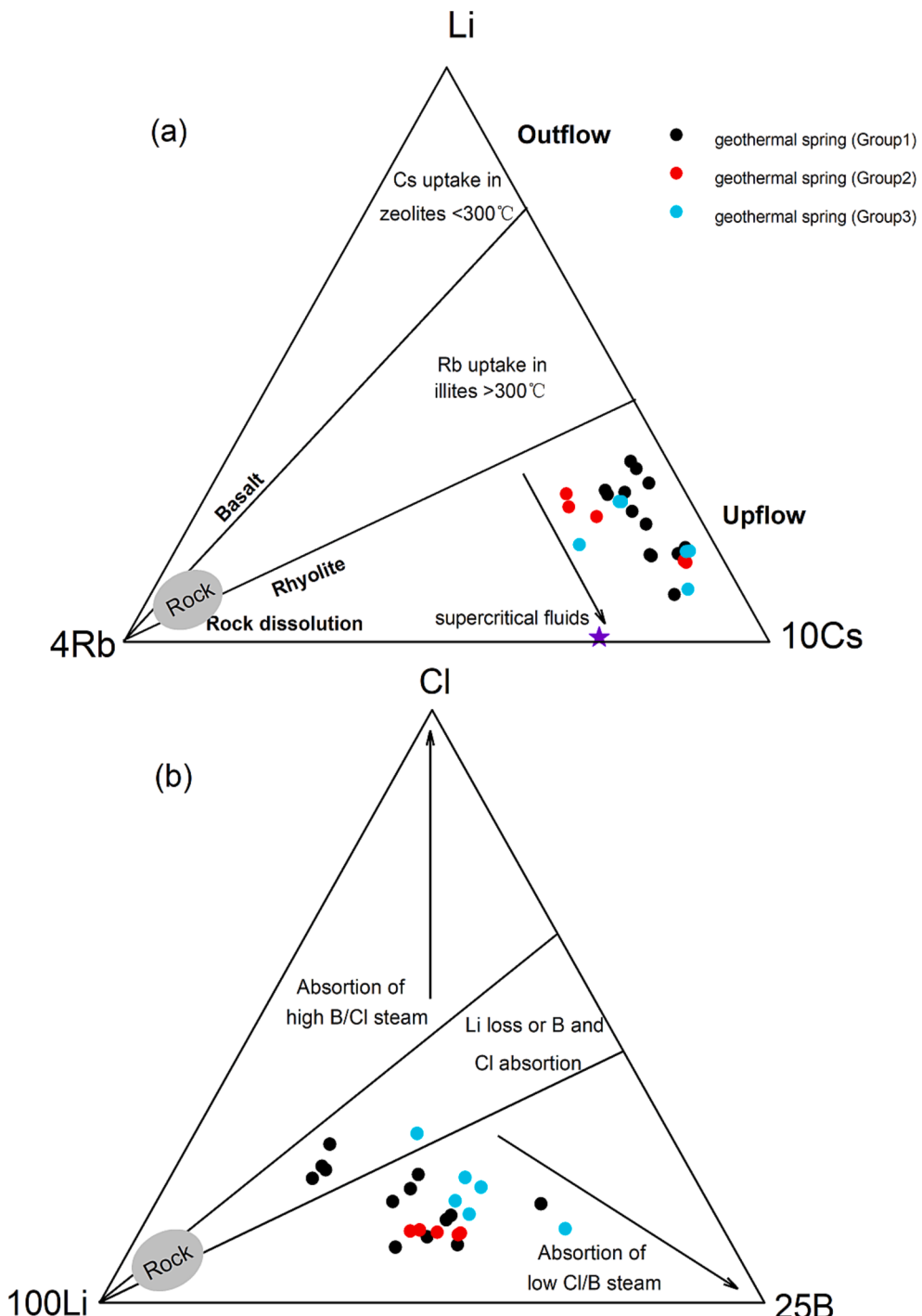


Fig. 7. Relative concentrations of (a) Li, Rb, and Cs; and (b) Cl, Li, and B of geothermal springs in the YGR.

geothermal waters dominated by volcanic rocks, the  $C_{\text{carb}}$  is close to zero which indicate the limited contribution of carbonate dissolution (Frondini et al., 2009). The  $\delta^{13}\text{C}_{\text{carb}}$  value is set as 1.7 ‰ based on the average of 350 marine carbonate samples from the southern Tibetan Plateau (Hu et al., 2001; Li et al., 2005a). The external carbon can be established by the binary mixing model, as follows (Chiodini et al., 2000):

$$C_{\text{exter}} = C_{\text{org}} + C_{\text{deep}} \quad (15)$$

$$\delta^{13}\text{C}_{\text{exter}} \times C_{\text{exter}} = \delta^{13}\text{C}_{\text{org}} \times C_{\text{org}} + \delta^{13}\text{C}_{\text{deep}} \times C_{\text{deep}} \quad (16)$$

where  $\delta^{13}\text{C}_{\text{org}}$  and  $\delta^{13}\text{C}_{\text{deep}}$  are the  $\delta^{13}\text{C}$  compositions of organic carbon and deeply derived  $\text{CO}_2$ , respectively. The theoretical mixing curves are

established based on the organic carbon end-member ( $\delta^{13}\text{C}_{\text{org}} = -26\text{\textperthousand}$  with variable  $C_{\text{org}}$  values of 0.1–3.0 mmol/L) and the deep carbon end-member ( $\delta^{13}\text{C}_{\text{deep}} = 0\text{\textperthousand}$  with  $C_{\text{deep}} \geq 60$  mmol/L) (Chiodini et al., 2004; Williams et al., 2013).

In the model, the calculated  $P_{\text{CO}_2}$  and  $T_{\text{DIC}}$  (Table 3) are under the threshold values ( $P_{\text{CO}_2} < 1\text{ bar}$  and  $T_{\text{DIC}} < 69.5\text{ mmol/L}$ ), suggesting that the uncertainty of the model caused by calcite precipitation and/or  $\text{CO}_2$  degassing can be ignored (Chiodini et al., 2000). The  $C_{\text{exter}}$  vs.  $\delta^{13}\text{C}_{\text{exter}}$  plot (Fig. 9) indicates that all the geothermal waters fall within the evolution curves between the organic and deep carbon end-members. The dominant carbon sources for geothermal waters can ascribable to deeply derived  $\text{CO}_2$ , with the contribution range from 77% to 99%. The

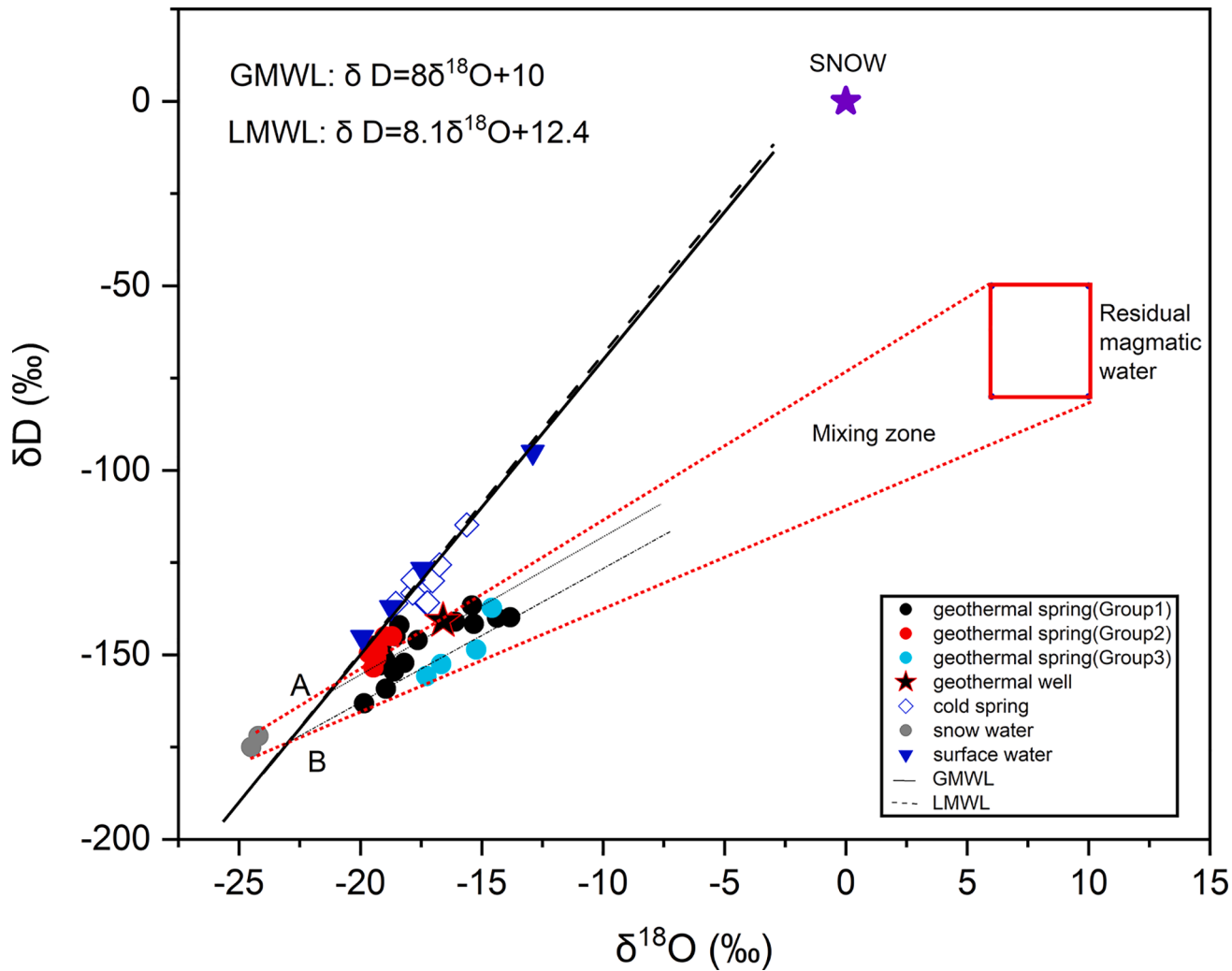


**Fig. 8.**  $\delta^{18}\text{O}$  vs.  $\delta\text{D}$  diagram of the geothermal springs, geothermal wells, cold springs and surface waters collected along the YGR. The black dashed line represents the global meteoric water line (GMWL; Craig, 1961), the black solid line represents the local meteoric water line (LMWL; Tan et al., 2014). Rectangle area represents residual magmatic water (water left after crystallization of the magma) distribution with the range of  $\delta^{18}\text{O}=6\text{--}9\text{ ‰}$ ,  $\delta\text{D}=-50\text{ -- }-80\text{ ‰}$  (after Taylor 1992).

geothermal waters in the southern segment are closer to the deep carbon end-member, which is consistent with the large-scale distribution of the metamorphic core complexes (i.e., Kangma gneiss dome) and/or the relatively shallow partial melting (Zhang et al., 2021; Xie et al., 2021).

#### 5.4. Reservoir temperature, cooling process, and circulation depth

##### 5.4.1. Empirical chemical geothermometers

Empirical chemical geothermometers, including cation and silica geothermometers, have been widely used to calculate subsurface geothermal reservoir temperatures and they are of pivotal importance to the exploration and development of geothermal resources (Kharaka and Mariner, 1989; Yang et al., 2019; Wu et al., 2021). Based on empirical or semi-empirical laws, chemical geothermometers rely on several assumptions including the existence of water-rock equilibrium, the adequate supplement of chemical species involved, and no significant modification of chemical composition (i.e., dilution, boiling, and re-equilibration) in upflow zones (Fournier and Truesdell, 1973; Fournier, 1977; Nicholson, 1993; Arnorsson, 2000). For a comprehensive understanding of the reservoir temperature, several chemical geothermometers are applied to verify or disprove the validity of the assumptions.

Before calculating the reservoir temperature, the water-rock equilibrium state should be determined first. The Na-K-Mg triangle plot

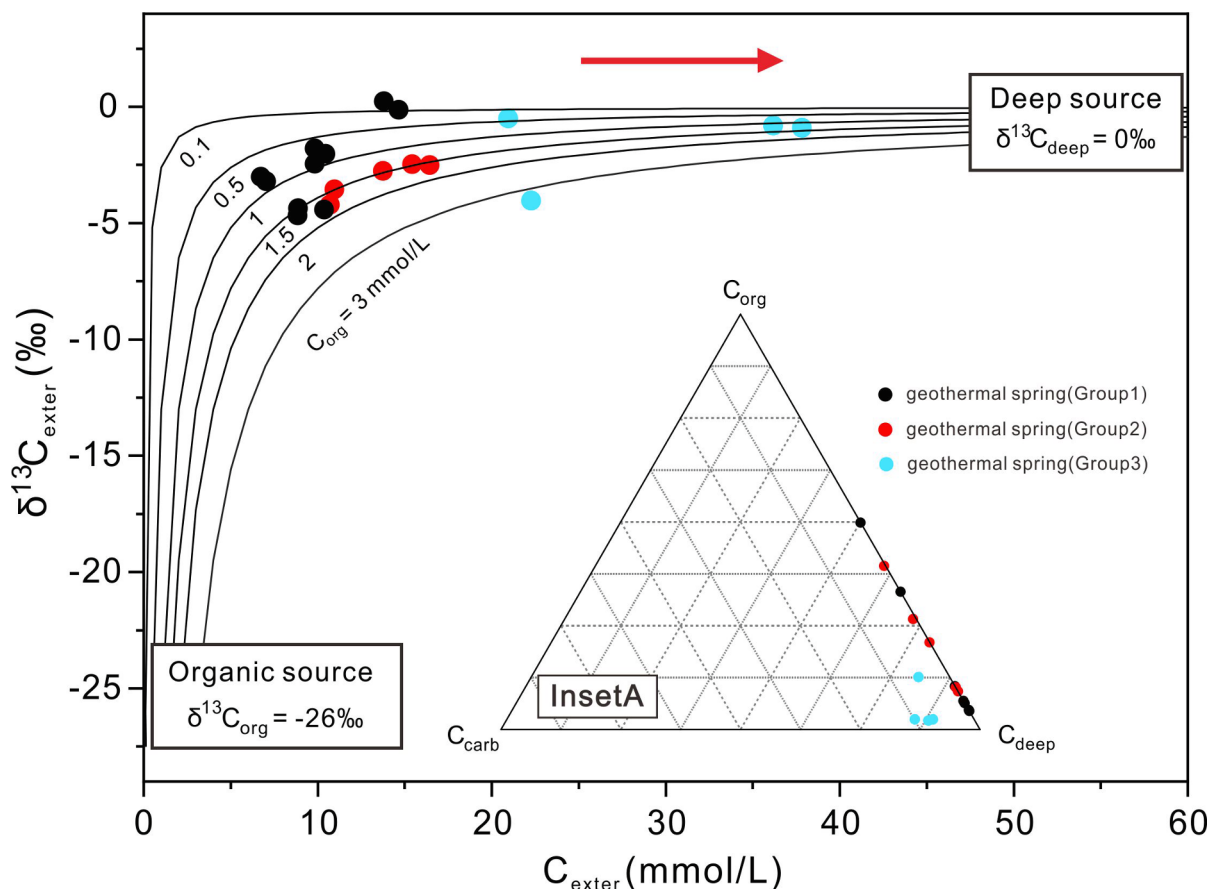
(Fig. 10a) proposed by Giggenbach (1988) have been widely used to determine the equilibrium state, the mixing degree, and the suitability of various cation geothermometers (e.g., Chao et al., 2021; Mao et al., 2021; Wu et al., 2021). Three groups are included: fully equilibrated, partially equilibrated, and immature waters. Fig. 10a shows that most geothermal springs from Group 1 (GL, YBJ, and YY geothermal fields), Group 2 (GRQ geothermal fields), and Group 3 (JZ geothermal field) fall into partially equilibrated areas, suggesting that water-rock equilibrium is generally occurred and the above samples are suitable for the application of cation geothermometers. Geothermal springs in the NZ (Group 1), YL (Group 2), and KM (Group 3) geothermal fields pertain to immature water which can be attributed to mixing with Mg-rich cold waters, shallow circulation depth and rapid flow rate (Giggenbach, 1988; Yang et al., 2017; Li et al., 2021). These immature waters may cause significantly over- or under-estimated temperatures through cation geothermometers.

Distinct differences are observed among the estimated temperatures for geothermal springs based on different cation geothermometers (Table 4 and Fig. 10b). Compared to the measure temperatures of geothermal wells (Fig. 10b), the Na-K-Ca geothermometer gives anomalously high temperature (310–525 °C), Mg-involving geothermometer gives relatively lower temperatures (81–259 °C), and the Na-Li geothermometer gives wide range of temperatures (119–475 °C). The Na-K geothermometer, which generally maintain deep equilibration

**Table 3**

Carbon balance results of geothermal springs along the YGR.

Group	Location	Sample ID	T <sub>DIC</sub> <sup>a</sup> mmol/L	Log (P <sub>CO<sub>2</sub></sub> ) <sup>a</sup> Log bar	δ <sup>13</sup> C <sub>TDIC</sub> ‰VPDB	C <sub>exter</sub> mmol/L	δ <sup>13</sup> C <sub>exter</sub> ‰VPDB	Contribution (%)	C <sub>deep</sub>	C <sub>org</sub>	C <sub>carb</sub>
The Northern segment											
Group1	Gulu	S01	14.67	-2.81	-0.14	14.67	-0.14	99	1	0	
		S02	13.80	-2.87	0.24	13.80	0.24	99	1	0	
	Ningzhong	S10	9.84	-2.48	-2.46	9.84	-2.46	93	7	0	
		S11	9.82	-2.03	-1.79	9.82	-1.79	93	7	0	
		S12	10.45	-1.84	-2.03	10.45	-2.03	93	7	0	
		S14	7.05	-2.20	-3.00	7.05	-3.00	89	11	0	
		S15	6.75	-1.91	-3.02	6.75	-3.02	88	12	0	
	Yangyi	S22	8.85	-2.52	-4.68	8.85	-4.68	83	17	0	
		S23	8.88	-2.09	-4.37	8.88	-4.37	83	17	0	
		S24	10.38	-1.94	-4.42	10.38	-4.42	84	15	0	
Group2	Yuela	S05	16.68	-0.81	-2.20	16.43	-2.26	89	9	1	
		S06	15.94	-1.39	-2.15	13.74	-2.76	77	9	14	
	Gariqiong	S07	15.80	-1.25	-2.38	15.44	-2.47	88	9	2	
		S18	10.71	-1.43	-4.22	10.71	-4.22	86	14	0	
		S19	10.97	-1.28	-3.56	10.97	-3.56	86	14	0	
The Southern segment											
Group3	Jiangzai	S26	23.20	-0.38	-0.29	20.95	-0.50	88	2	10	
	Kangma	S28	41.29	-0.04	-0.51	36.18	-0.82	85	2	12	
		S29	41.38	-0.03	-0.68	37.83	-0.91	89	2	9	
		S31	23.82	-0.34	-3.67	22.27	-4.04	81	13	7	

<sup>a</sup> Modelled based on PHREEQC (Parkhurst and Appelo, 2013).

**Fig. 9.** Mixing model of  $\delta^{13}\text{C}_{\text{exter}}$  versus  $\text{C}_{\text{exter}}$  for geothermal springs along the YGR. Model curves (black solid lines) that encompass most geothermal springs connected empirical end members ( $\delta^{13}\text{C}_{\text{org}} = -26\text{\textperthousand}$ ,  $\text{C}_{\text{org}} = 0.1\text{-}3 \text{ mmol/L}$ ;  $\delta^{13}\text{C}_{\text{deep}} = 0\text{\textperthousand}$ ,  $\text{C}_{\text{deep}} \geq 60 \text{ mmol/L}$ ). InsetA: The calculated percentages of the difference sources of  $\text{CO}_2$  based on water chemistry.

temperature for slow kinetics of Na-K equilibration and insensitive to secondary processes (Giggenbach, 1988; Delalande et al., 2011; Rezaei et al., 2019), provides more reliable results (202–321 °C) for geothermal

waters generally attain water-rock equilibrium.

The SIs (Table 5) suggest that the quartz/chalcedony equilibria are generally established for all the geothermal springs and silica

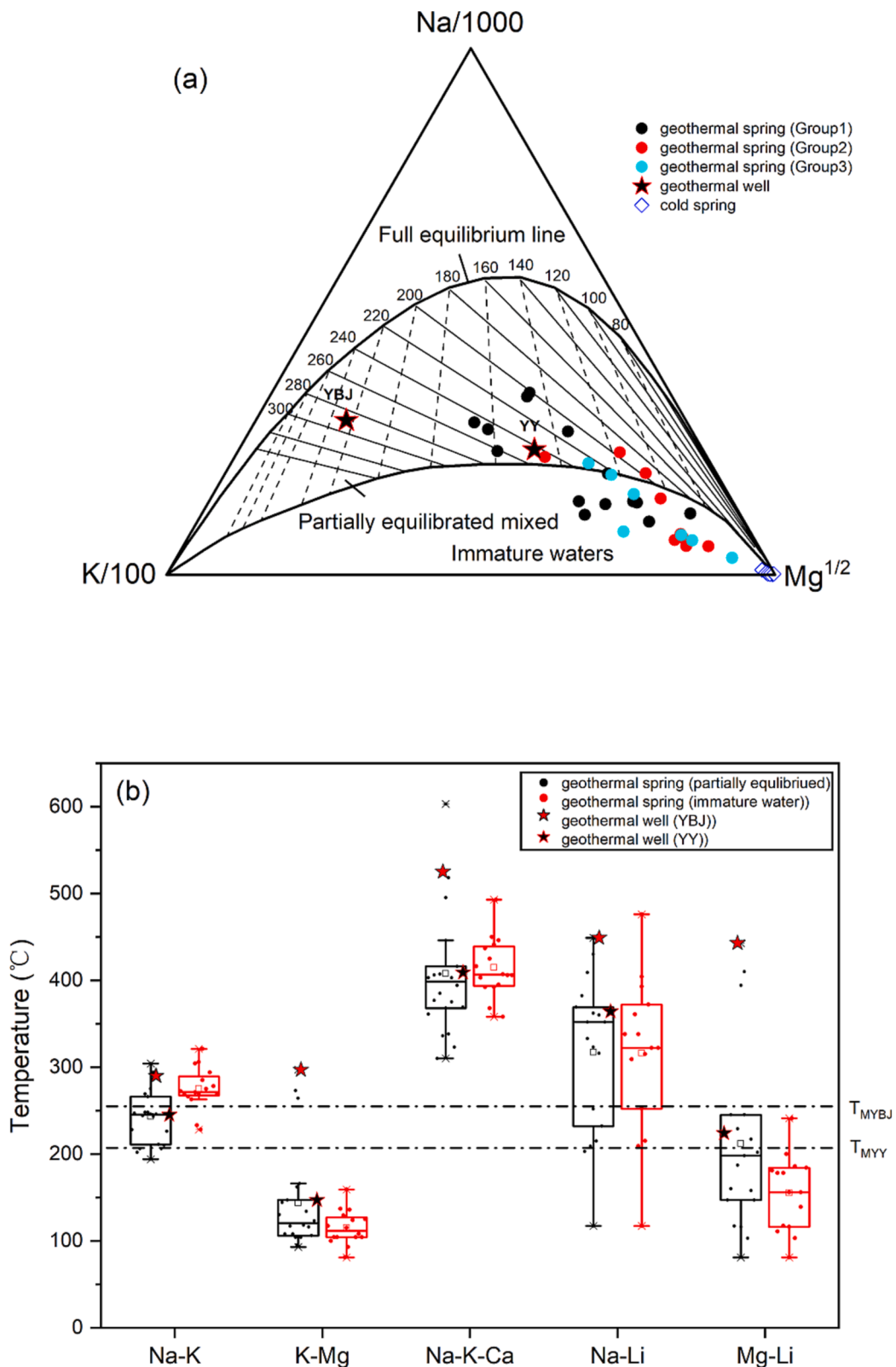


**Fig. 10.** (a) The Na-K-Mg ternary diagram (Giggenbach, 1988) and (b) Box and whisker plots of the geothermal springs, geothermal wells and cold springs in the YGR.  $T_{\text{MYBJ}}$  and  $T_{\text{MYY}}$  are measured temperatures of YBJ and YY geothermal wells, respectively.

geothermometers are suitable for the study region. Temperatures estimates with quartz without steam loss, quartz with complete steam loss, and improve-SiO<sub>2</sub> geothermometers are similar to each other with average values of 149 °C, 142 °C, 149 °C, respectively; while those with

chalcedony geothermometer are relatively low with the average values of 124 °C (Table 4). Silica geothermometers provide relatively lower temperatures than Na-K geothermometer.

**Table 4**

Equilibrium temperature estimated by selected chemical geothermometers.

Group	Location	Sample ID	Cation geothermometer					Silica geothermometer				Circulation Depth (km)
			Na-K <sup>a</sup>	K-Mg <sup>b</sup>	Na-K-Ca <sup>c</sup>	Na-Li <sup>d</sup>	Mg-Li <sup>e</sup>	Quartz (no loss) <sup>f</sup>	Quartz (max loss) <sup>g</sup>	Chalcedony <sup>h</sup>	Improved SiO <sub>2</sub> <sup>i</sup>	
The Northern segment												
Group1	Gulu	S01	246	259	519	358	383	161	153	138	161	2.45-2.87
		S02	249	165	509	352	243	158	150	134	158	
		S03	243	-	-	357	-	160	152	136	160	
		S04	248	162	446	323	229	144	138	118	144	
		S10	270	115	442	315	156	154	147	129	154	5.05-5.78
Group1	Ningzhong	S11	271	129	425	334	177	154	147	129	154	
		S12	305	136	492	395	187	154	147	130	154	
		S13	285	137	446	321	178	152	145	127	152	
		S14	260	174	428	403	264	159	151	135	159	
		S15	229	125	393	361	201	163	154	139	163	
	Yangbajing	S16	245	118	401	432	199	167	157	144	167	5.20-6.69
		S17	243	117	384	378	186	169	159	146	169	
		W01	290	225	525	449	333	267	237	263	-	
		S22	209	134	337	332	217	196	181	178	197	5.19-6.85
		S23	206	95	376	316	159	196	182	178	197	
Group2	Yuela	S24	206	147	335	351	244	197	182	178	197	
		S25	202	166	377	409	297	186	173	165	186	
		W02	244	148	408	356	222	228	206	215	-	
		S05	275	104	407	119	81	117	116	89	118	3.50-4.67
		S06	303	104	402	253	117	119	117	90	119	
	Gariqiong	S07	267	104	408	215	117	119	118	91	120	
		S08	294	108	416	-	-	118	117	90	118	
		S09	268	93	367	211	104	146	140	120	146	
		S18	194	117	310	212	161	131	128	104	131	4.15-4.62
		S19	195	109	311	205	148	137	132	110	137	
		S20	215	107	331	236	147	140	135	114	140	
		S21	247	144	394	-	-	130	127	103	130	
The Southern segment												
Group3	Jiangzi	S26	225	123	361	369	202	148	142	123	148	5.60-6.47
		S27	228	130	369	-	-	145	139	119	145	
		S28	277	81	405	310	111	111	111	82	112	3.40-6.50
	Kangma	S29	272	86	395	323	122	107	107	78	108	
		S30	-	-	-	-	-	97	98	67	98	
		S31	269	105	392	372	156	92	94	62	93	
		S32	233	117	358	335	181	84	87	53	85	
		S33	321	125	450	475	184	100	101	70	101	

Note: All concentrations are given in mg/L; S is the concentration of SiO<sub>2</sub> in mg/L. - = not analyzed.<sup>a</sup> Giggenbach (1988), T<sub>Na-K</sub> = 1390/[1.75+lg(Na/K)]-273.15.<sup>b</sup> Giggenbach (1988), T<sub>K-Mg</sub> = 4410/[(14.0+lg(K<sup>2</sup>/Mg)]-273.15.<sup>c</sup> Fournier and Truesdell(1973), T<sub>Na-K-Ca</sub> = 1647/[lg(Na/K)+βlg(√Ca/Na)+2.24]-273.15, β = 4/3 if T < 100 °C and lg(√Ca/Na) > 0 , β = 1/3 if T > 100 °C and for lg(√Ca/Na) < 0.<sup>d</sup> Verma and Santoyo (1997), T<sub>Na-Li</sub> = 1049/[lg(Na/Li)+0.44]-273.15 where Cl < 0.3 mol/L; T<sub>Na-Li</sub> = 1267/[lg(Na/Li)+0.07]-273.15 where Cl > 0.3mol/L.<sup>e</sup> Kharaka and Mariner (1989), T<sub>Mg-Li</sub> = 2200/[log(√Mg/Li) + 5.47] -273.15.<sup>f</sup> Fournier (1977), T<sub>SiO<sub>2</sub></sub> = [1309/(5.19-lgS)] - 273.15, without steam loss.<sup>g</sup> Fournier (1977), T<sub>SiO<sub>2</sub></sub> = [1522/(5.75-lgS)] - 273.15, with maximum steam loss.<sup>h</sup> Fournier (1977): T<sub>SiO<sub>2</sub></sub> = [1032/(4.69-lgS)]-273.15.<sup>i</sup> Verma and Santoyo (1997), T<sub>SiO<sub>2</sub></sub> = -44.119+0.24469S-1.7414×10<sup>-4</sup>S<sup>2</sup>+79.305lgS, where S < 295 mg/L.

#### 5.4.2. Mixing model and ratio

The characteristics of conservative elements ratios (i.e., Cl/B ratio), oxygen and hydrogen isotopes, and chemical geothermometers discussed above indicate the possible mixing process of the YGR (Fournier, 1979; Arnorsson, 2000). The Si-Enthalpy mixing method (Truesdell and Fournier, 1977), which can recognize the mixing processes and mixing ratios, is used as a supplement method to estimate reservoir temperature.

In the Si-Enthalpy mixing model (Fig. 11), two methods are applied for mixed groundwaters under the conditions that steam loss occurs or not before mixing. Assuming no steam loss before mixing, the mixing line (joining cold springs to geothermal springs) intersect the quartz solubility curve indicate the reservoir temperature. For geothermal springs in Group 1, Group 2, and Group 3, reservoir temperatures are in the range of 196-302 °C (N<sub>1</sub>-N<sub>2</sub>), 164-207 °C (C<sub>1</sub>-C<sub>2</sub>), and 137-261 °C (S<sub>1</sub>-S<sub>2</sub>), respectively. If steam loss from adiabatically cooled fluid before mixing, the intersection points N<sub>3</sub>-N<sub>4</sub>, C<sub>3</sub>-C<sub>4</sub>, and S<sub>3</sub>-S<sub>4</sub> demonstrate

reservoir temperatures for Group 1, Group 2 and Group 3 are in the range of 134-151 °C, 122-133 °C, and 112-144 °C, respectively. The Si-Enthalpy mixing model suggests that there are at least two reservoirs with different temperatures. According to the drilling data, two types of geothermal reservoirs (including intermediate temperature and high temperature) exist in the northern part of the YGR with the measure temperatures of < 172 °C and 190 – 207 °C for YY geothermal field and 130-173 °C and 330 °C for YBJ geothermal field (Zhao et al., 1998; Dor, 2003; Wang et al., 2018a). Thus, the temperatures estimated by the assumptions that no loss before mixing give more reasonable results.

There's no intersection point from the cold spring to the geothermal wells (in the YBJ and YY geothermal fields) with the quartz solubility curve, suggesting the mixing process is not the major cooling process. The intersection points of A and B indicate the reservoir temperature without steam loss for YY and YBJ geothermal fields, i.e., 205 °C and 250 °C, respectively. The reservoir temperature of YBJ geothermal well by Si-Enthalpy mixing model is lower than multiple chemical

**Table 5**

The speciation calculations of geothermal springs, geothermal wells and cold springs based on PHREEQC.

Location	Sample ID	Halite	Aragonite	Calcite	Dolomite	Chalcedony	Quartz	Anhydrite	Gypsum	Fluorite	LogP <sub>CO<sub>2</sub></sub>
The Northern segment											
Gulu	S01	-4.8	-0.3	-0.2	0.5	0.0	0.3	-5.1	-5.4	-3.0	-2.81
	S02	-4.8	0.0	0.1	1.6	0.0	0.2	-5.0	-5.4	-1.8	-2.87
	S03	-4.7	-1.4	-1.3	-0.6	-0.1	0.1	-5.4	-5.7	-3.4	-2.9
	S04	-4.8	0.6	0.8	1.7	0.2	0.4	-3.8	-4.1	-0.6	-1.51
	G01	-10.0	0.0	0.2	0.3	0.4	0.7	-2.1	-1.8	-	-3.18
Yuela	S05	-6.2	-0.2	-0.1	-0.3	0.4	0.6	-2.4	-2.5	-1.0	-0.81
	S06	-6.6	1.0	1.1	1.5	0.4	0.7	-2.3	-2.3	-0.4	-1.39
	S07	-6.5	0.1	0.3	0.7	0.3	0.6	-3.0	-3.1	-1.2	-1.25
	S08	-6.6	1.1	1.2	2.2	0.2	0.4	-2.4	-2.6	-0.8	-1.82
	S09	-6.6	0.7	0.8	1.3	0.4	0.7	-1.7	-2.0	-0.8	-0.84
	G02	-11.4	-0.2	0.0	0.7	0.3	0.6	-3.1	-2.7	-	-2.93
	G03	-9.0	-0.2	0.0	0.6	1.0	1.3	-2.8	-2.5	-	-3.22
Ningzhong	S10	-5.3	1.1	1.3	3.2	0.2	0.4	-2.1	-2.5	-1.3	-2.48
	S11	-5.3	1.1	1.3	2.4	0.3	0.5	-1.7	-2.0	-0.5	-2.03
	S12	-5.4	0.6	0.7	1.7	0.3	0.5	-2.1	-2.5	-1.0	-1.84
	S13	-5.2	1.4	1.5	2.8	0.2	0.4	-1.4	-1.8	-0.5	-2.11
	S14	-5.8	0.2	0.4	-0.1	0.1	0.4	-3.2	-3.6	-1.2	-2.20
	S15	-5.9	-0.2	-0.1	0.0	0.2	0.4	-3.2	-3.6	-1.5	-1.91
	G04	-9.8	-2.3	-2.2	-3.6	0.7	0.9	-3.6	-3.2	-	-2.67
	G05	-9.7	-1.1	-0.9	-1.1	0.7	1.0	-3.4	-3.1	-	-2.66
Yangbajing	S16	-5.4	0.7	0.8	1.8	0.3	0.5	-2.4	-2.8	-0.4	-2.77
	S17	-5.4	0.8	0.9	1.7	0.3	0.6	-2.3	-2.7	-0.1	-1.87
	W01	4.7	0.4	0.6	0.8	0.3	0.4	-2.4	-3.3	0.8	2.43
	G06	-9.8	-0.7	-0.6	-1.0	0.5	0.8	-3.0	-2.7	-	-3.68
	G07	-11.6	-0.7	-0.6	-0.9	0.6	0.9	-3.3	-3.0	-	-3.34
Gariqiong	S18	-6.2	0.7	0.8	0.7	0.2	0.4	-2.2	-2.5	-0.1	-1.43
	S19	-6.3	0.4	0.5	0.4	0.3	0.5	-2.1	-2.4	-0.2	-1.28
	S20	-6.4	0.6	0.8	1.0	0.3	0.5	-2.3	-2.7	-0.2	-1.37
	S21	-6.2	0.4	0.5	0.3	0.2	0.4	-2.3	-2.6	-	-1.22
	G08	-6.4	0.3	0.5	1.3	0.4	0.7	-1.7	-1.3	-	-3.20
Yangyi	S22	-5.8	1.2	1.4	1.8	0.5	0.7	-1.9	-2.2	-	-2.52
	S23	-5.8	-0.1	0.1	1.3	0.6	0.8	-2.8	-3.1	-0.5	-2.09
	S24	-5.8	1.0	1.1	1.4	0.6	0.8	-1.8	-2.1	-1.6	-1.94
	S25	-5.8	0.0	0.2	1.0	0.4	0.6	-3.0	-3.4	-0.4	-2.45
	W02	-5.7	0.5	0.7	0.9	0.7	0.9	-2.0	-2.4	-0.6	-1.76
The Southern segment											
Jiangzi	S26	-4.6	0.2	0.4	0.2	0.5	0.7	-2.4	-2.6	-0.2	-0.38
	S27	-4.5	0.8	0.9	1.3	0.4	0.6	-2.3	-2.5	-0.2	-0.75
	G09	-9.8	0.1	0.2	1.4	0.5	0.8	-2.2	-2.0	-	-3.28
Kangma	S28	-5.5	-0.9	-0.7	0.4	0.6	0.8	-3.4	-3.4	-2.6	-0.04
	S29	-5.5	-0.8	-0.6	0.3	0.5	0.8	-3.0	-2.9	-	-0.03
	S30	-5.4	0.1	0.2	-0.5	0.6	0.8	-2.5	-2.4	-0.1	-0.64
	S31	-5.5	-0.7	-0.5	-0.1	0.3	0.6	-3.2	-3.2	-0.5	-0.34
	S32	-5.5	-0.7	-0.5	-0.1	0.3	0.6	-3.2	-3.2	-0.3	-1.09
	S33	-4.9	1.7	1.8	3.0	0.2	0.4	-3.2	-3.3	-0.6	-1.81
	G10	-9.4	-0.8	-0.7	-0.8	0.5	0.7	-1.5	-1.3	-	-2.21
	G11	-9.7	0.5	0.6	2.1	-0.1	0.1	-1.9	-1.6	-	-3.09
	G12	-9.5	-1.9	-1.8	-3.0	0.4	0.7	-2.4	-2.0	-	-2.77

geothermometers and maximal measured temperature of drilling well (330 °C), owing to the SiO<sub>2</sub> re-equilibrium during the ascending process (Zhao et al., 1998). The estimated temperature of YY geothermal well by Si-Enthalpy is generally consistent with the measured temperature (207 °C), suggesting the limited contribution by secondary processes. This is also confirmed by some geothermal springs in the YY, whose mixing line fail to intersect to the quartz solubility curve.

Fig. 11 suggests that most geothermal springs are formed by the mixing of deep geothermal water and shallow groundwater or surface water. Assuming that the dissolved SiO<sub>2</sub> was saturated in the deep geothermal fluid, the proportion of the mixed water can be expressed as follows (Truesdell and Fournier, 1977):

$$E_{cw}X + E_h(1-X) = E_S \quad (17)$$

$$Si_{cw}X + Si_h(1-X) = Si_S \quad (18)$$

where E<sub>cw</sub> is the enthalpy of the cold water, E<sub>h</sub> is the enthalpy of the deep geothermal fluid, E<sub>S</sub> is the final enthalpy of the geothermal spring, Si<sub>cw</sub> is the SiO<sub>2</sub> concentration of the cold spring, Si<sub>h</sub> is the SiO<sub>2</sub>

concentration of the deep geothermal fluid, Si<sub>S</sub> is the SiO<sub>2</sub> concentration of the geothermal spring, and X is the mixture ratio of cold water with the deep geothermal fluid. Based on a graphical method, the cold waters mixing ratios of the different geothermal fields in the YGR are plotted on the Fig. 12. Calculated proportions of cold waters for the geothermal springs in Group 1, Group 2, Group 3 are in the range of 64–66%, 69–76%, and 78–81%, respectively.

#### 5.4.3. Geothermometrical modelling

Geothermometrical modelling depends on solid thermodynamic basis and complete fluid compositions. It can provide the convergence of multi-mineral equilibrium and has been proven to give effective prediction of reservoir temperatures (Reed and Spycher, 1984; Pang and Reed, 1998; Palandri and Reed, 2001; Guo et al., 2017; Wang et al., 2021). The “FixAl” method, which considered the influence of degassing/mixing processes and errors of Aluminum analysis for multi-mineral equilibrium, was applied to reconstruct the conditions of deep reservoirs based on SOLVEQ-XPT code (Pang and Reed, 1998; Reed et al., 2012). Degassed CO<sub>2</sub> was re-established by adding equal moles of H and HCO<sub>3</sub> with the

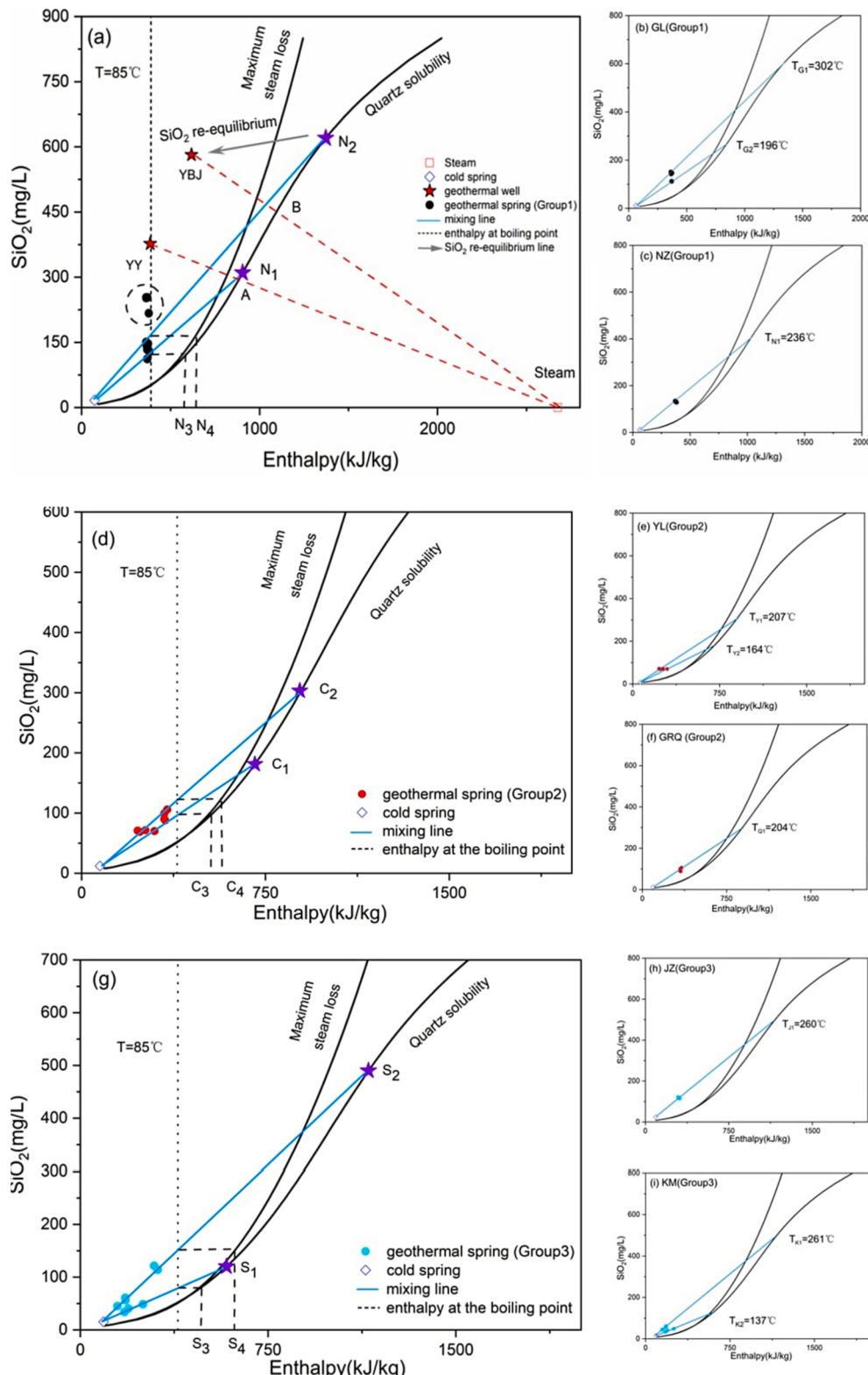


**Fig. 11.** Silica-enthalpy mixing model of geothermal waters in (a) Group1, (d) Group2, (g) Group3, and corresponding detailed conditions of (b) GL, (c) NZ, (e) YL, (f) GRQ, (h) JZ, and (i) KM geothermal fields along the YGR.

range of 0.1–0.9 mol/L, and mixing process was corrected by removing corresponding moles  $\text{H}_2\text{O}$  related to the calculated mixture ratio (Fig. 13). To eliminate the erroneous or lacking analyses of Al, albite was selected as Al-bearing mineral to force equilibrium in the systems (Pang and Reed, 1998). The mineral sets were selected based on hydrochemical

characteristics, hydrothermal alteration minerals and aquifer lithology (Zhu and Xu, 1989; Hou et al., 2015). Geothermal water with the highest sampling temperature was chosen to represent each geothermal field. Predicted reservoir temperatures with reconstructed mineral equilibrium are plotted as Fig. 13. Reservoir temperatures for geothermal waters of

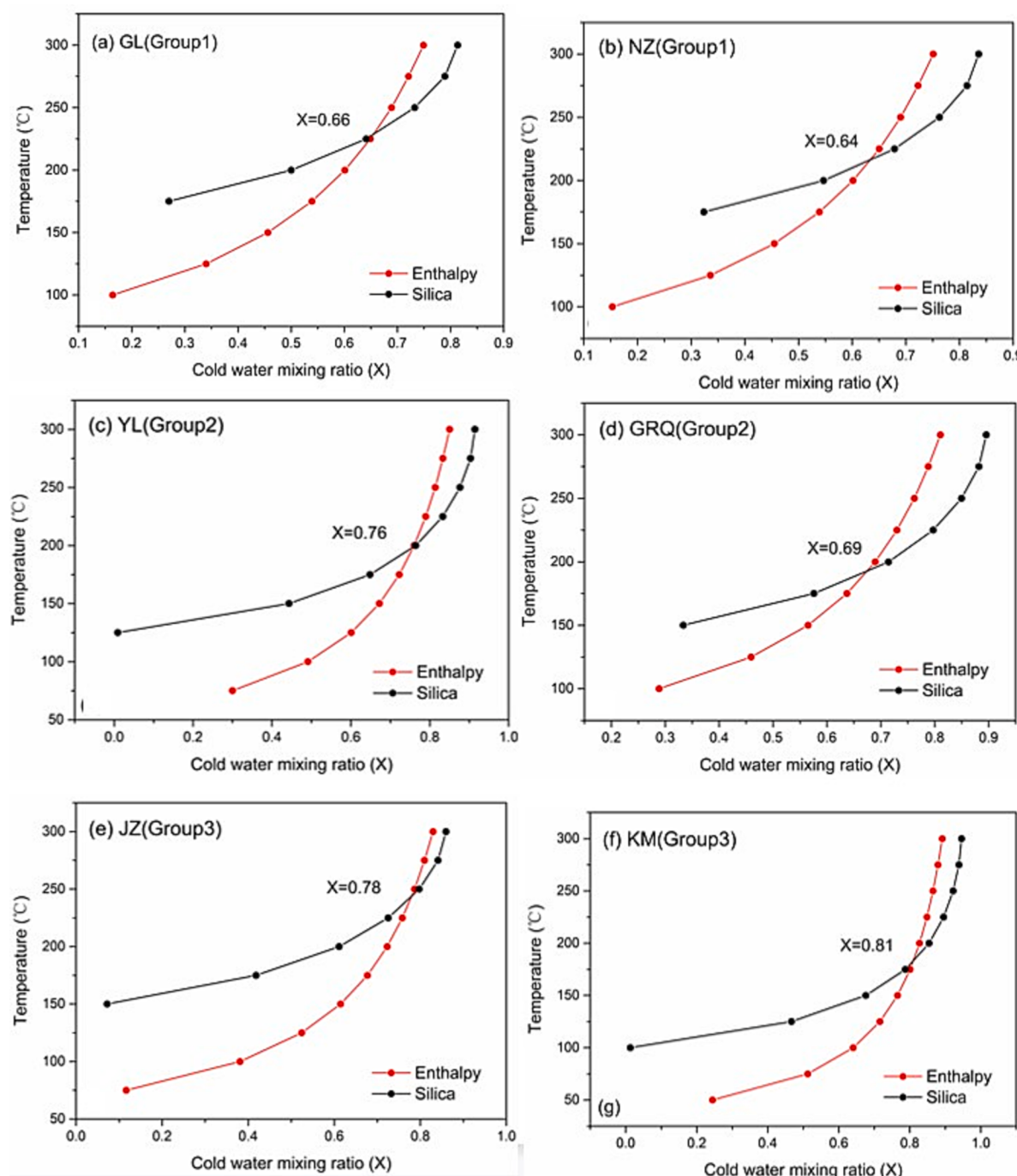


**Fig. 12.** The proportions of cold waters before mixing for the mixed geothermal waters along the YGR.

Group 1, Group 2 and Group 3 are in the range of 249–312 °C, 216–218 °C, and 235–238 °C, respectively. Meanwhile, the molded pH of geothermal waters in the deep reservoir are slightly acidic ( $\text{pH}=5.8\text{--}6.4$ ) with the degassed  $\text{CO}_2$  ranging from 0.1–0.9 mol/L. This suggests after varying degrees of  $\text{CO}_2$  escaped during the ascending process, the deep geothermal waters elevated to slightly acidic and alkaline ( $\text{pH}=6.1\text{--}9.1$ ) at the surface. The estimated temperatures by geothermometrical modelling are generally consistent with that from Na-K geothermometer and Si-Enthalpy mixing model for partially equilibrated geothermal waters. For immature waters, geothermometrical modelling gives consistent results with Si-Enthalpy mixing model but not with empirical chemical geothermometers.

#### 5.4.4. Circulation depth

According to the temperature estimated by various geothermometers, mixing model and geothermometrical modelling, the circulation depths of geothermal springs can be calculated as follows (Yang et al., 2017; Qiu et al., 2018):

$$D = H_{cz} + (T_e - T_a)/G_g \quad (19)$$

where  $D$  is the maximum circulation depth of geothermal waters (m);  $H_{cz}$  is the thickness of the constant temperature zone (m);  $T_e$  is the calculated reservoir temperature (°C);  $T_a$  is the temperature of the normal temperature zone (°C);  $G_g$  is the local geothermal gradient (°C/km). The thickness of the constant temperature zone is 20 m (Liu et al., 2022); the local average temperature is -2 °C; the geothermal gradients

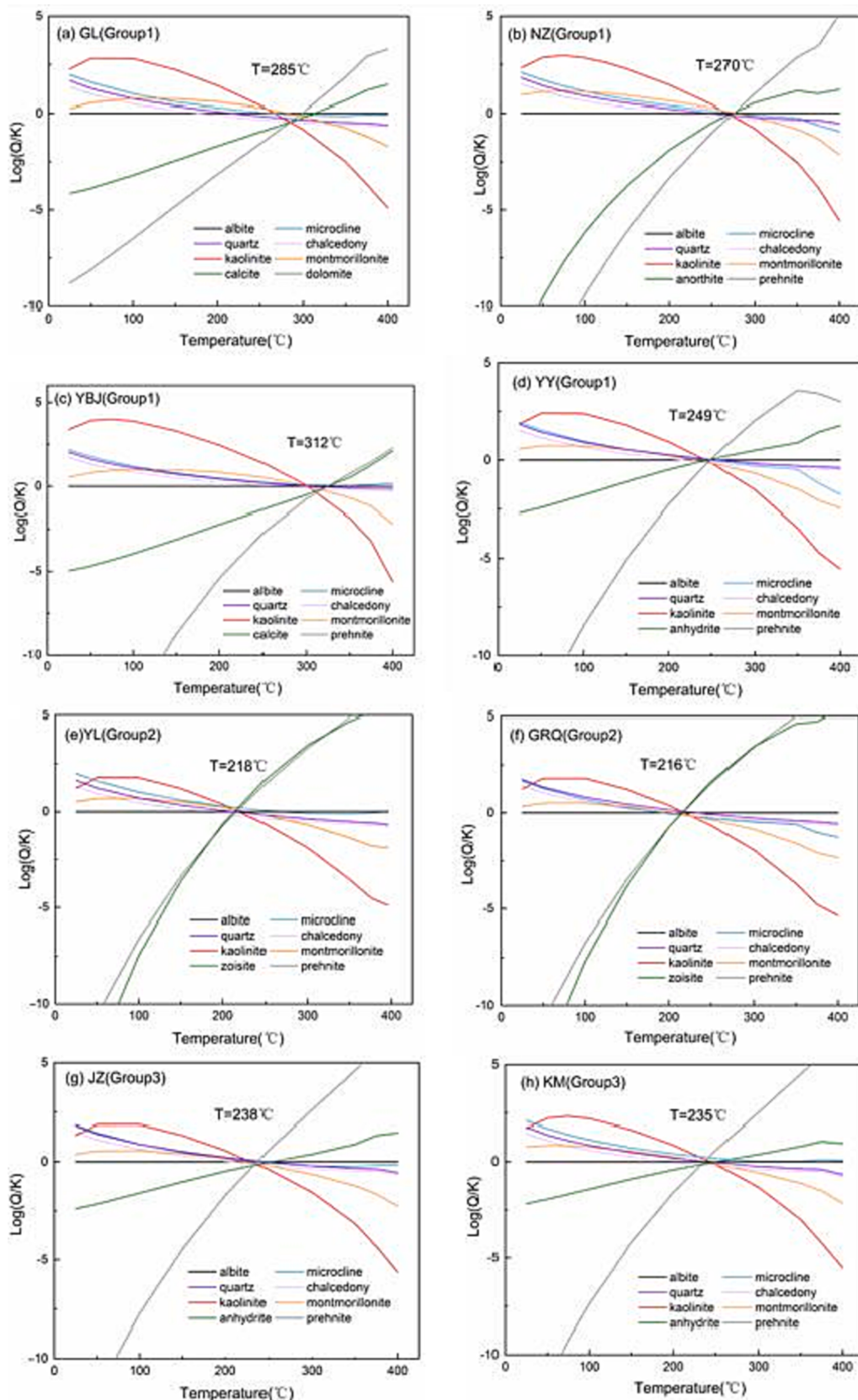


**Fig. 13.** FixAl graph of reconstructed mineral equilibrium and predicted reservoir temperatures for representative geothermal waters in eight geothermal fields along the YGR.

are based on the measured drilling data (Jiang et al., 2016). As shown in the Table 4, the circulation depths for the northern segment and southern segment are in the range of 2.45–6.85 km and 3.40–6.50 km, respectively.

## 6. Conceptual model and evolution of geothermal water

Based on the geomorphologic setting, geochemical characteristics, and isotopic signature, the conceptual model of the mediate-high temperature geothermal systems in the YGR across southern Tibetan Plateau was proposed (Fig. 14). In the YGR, a non-volcanic area with the magmatic heat source, the dominated recharge sources of geothermal waters are the combination of meteoric water, snow-melt water, and magmatic fluids. The meteoric water and/or snow-melt water from the surrounding mountains (Nyencheng Tanglha mountains/Himalayan mountains) infiltrated deeply under the driving force of >1000 m water-head through a series of N-S-trending normal fault systems and E-W-stretching thrust systems. The crustal partial melting, which validated by multiple geophysical methods (i.e., magnetotelluric data, seismic wave data, and earthquake data), can be regarded as principally heat source to actuate the geothermal activities in the YGR (e.g., Makovsky et al., 1996; Kind et al., 1996; Unsworth et al., 2005; Xie et al., 2021). The deep circulating fluid mixing the magmatic fluid (about 14%–31%) to form highly reactive acid solutions, and further interacted with wall rocks result in neutral NaCl water (primary neutralization process) involving the precipitations of various alteration minerals (e.g., albite, calcite, kaolinite and microcline) (Giggenbach, 1988). The neutral NaCl waters ascended to the surface with the formation of several deep and/or shallow reservoirs formed with various reservoir temperatures (137–312 °C) at different depth (2.45–6.85 km). During the ascending processes, heated geothermal waters are cooled by adiabatic degassing, conductive cooling, and mixing with shallow cold water, as well as a combination of the above processes. Meanwhile, progressive water-rock interactions (i.e., silicate weathering, carbonate dissolution, and cation exchange) combining the increasingly CO<sub>2</sub>-rich vapor (about 0.1 mol/L–0.9 mol/L) generated Cl-HCO<sub>3</sub>-Na/HCO<sub>3</sub>-Cl-Na water (Group 1, Group 3) and HCO<sub>3</sub>-Na water (Group 2) with varying maturity degrees and complex chemical characteristics.

## 7. Conclusions

Geochemistry of major solutes, typical trace elements (Li, Rb, Cs, and B) and stable isotopes ( $\delta D$ ,  $\delta^{18}O$  and  $\delta^{13}C_{\text{TPIC}}$ ) of geothermal waters in the YGR were determined to investigate the major geochemical processes controlling the origin, evolution, and circulation mechanism. The cold springs and surface waters are consistently characterized by Ca-HCO<sub>3</sub> dominated waters with extremely low concentrations of trace elements. The geothermal springs present extensive variability and can be classified into three groups: Na-Cl dominated (Group 1) with high trace elements in the northern segment, Na-HCO<sub>3</sub> waters (Group 2) with relatively low trace elements in the northern segment, and Na-Cl dominated (Group 3) with abnormally high trace elements in the southern segment. The source of major solutes for cold springs and surface waters are dominated by carbonate dissolution, while that for geothermal springs are dominated by silicate weathering, carbonate dissolution and cation exchange. Typical trace elements are significantly depleted relative to the median rock ratios, and the ion ratios suggest the potential addition of B by magmatic degassing and similar deep processes of geothermal waters.

The recharge sources of geothermal springs are the combination of meteoric water, snow-melt, and magmatic fluid, while that for cold springs and surface waters are meteoric water. The Nyencheng Tanglha mountains and Himalayan mountains can be the main recharge sources of geothermal waters. Snow-melt waters and meteoric waters infiltrated deeply through a series of fault systems in the YGR and mixed with magmatic fluids with varying degree, i.e., Group 1, Group 2 and Group 3 with the range of 15–31%, 14–16% and 21–28%, respectively. The dominant carbon sources for geothermal waters can ascribable to deeply derived CO<sub>2</sub>, including magmatic source and metamorphic source, with the contribution range from 77% to 99%. The calculated subsurface temperatures are in the range of 137–312 °C, and belong to median-high temperature geothermal systems. The circulation depths for the northern and southern segments are in the range of 2.45–6.85 km and 3.40–6.50 km, respectively. The geothermal fields along the YGR have uniform heat source and undergo the combing cooling processes as well as multifarious water-rock interactions. This study can improve the understanding of the origin, evolution, and circulation of deep-circulating groundwater, and helpful for exploration

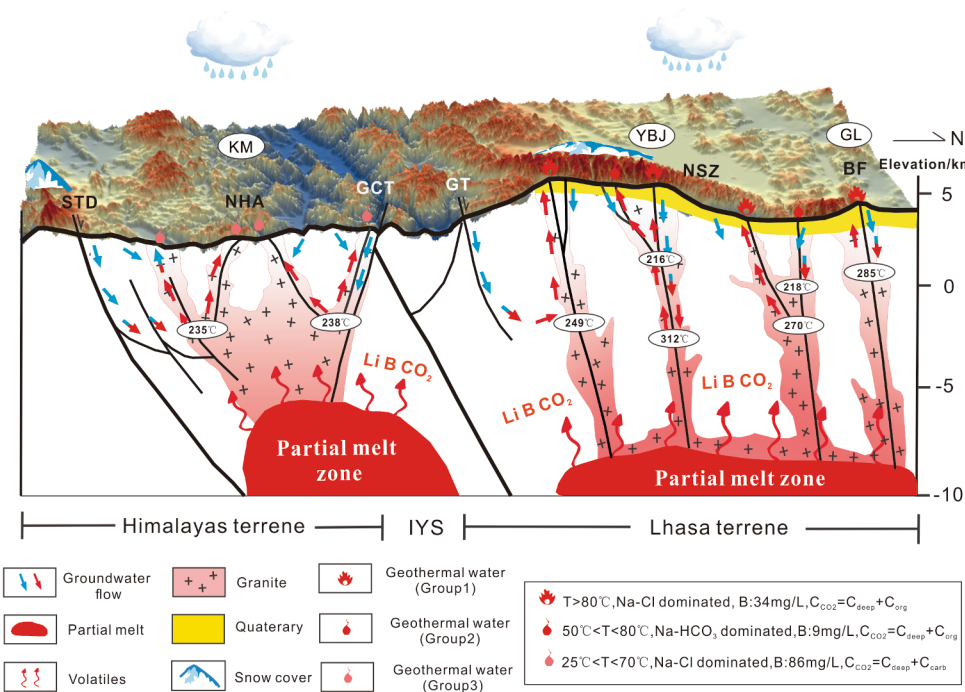


**Fig. 14.** The conceptual model of the Yadong-Gulu rift, Southwest China. Abbreviations: STD, the South Tibetan detachment system; NHA, Northern Himalayan anticline; GCT, Great counter thrust belt; IYS, Indus-Yarlung-Tsangpo suture; GT, Gangdese thrust belt; NSZ, Nyainqntanglha shear Zone; BF, Benguo strikeslip fault zone. Sources of the depths of partial melt (Brown et al., 1996; Unsworth et al., 2005). Sources of the locations of the faults: STD (Hauck et al., 1998; Li et al., 2015); NHA (Hauck et al., 1998); GCT and GT (Nelson et al., 1996; Yin and Harrison, 2000; Li et al., 2015); GT (Nelson et al., 1996); NSZ (Nelson et al., 1996; Cogan et al., 1998; Kapp et al., 2005); BF (Armijo et al., 1989; Wu et al., 2011). The concentrations of B are the average concentrations of the group. C<sub>CO2</sub> is the mainly source of the dissolved carbon.

and exploitation of the high-temperature geothermal resources.

## Declaration of Competing Interest

The authors declare that they have no known competing financial interests or personal relationships that could have appeared to influence the work reported in this paper.

## Data availability

Data will be made available on request.

## Acknowledgments

We thank for reviewers for their valuable comments and editor for efficient editorial handling. This study was supported by the National Natural Science Foundation of China (Grant No. 91747204 and No. 92047202), and High-level Special Funding of the Southern University of Science and Technology (Grant Nos. G02296302, G02296402).

## References

- Alsdorf, D., Nelson, D., 1999. Tibetan satellite magnetic low: Evidence for widespread melt in the Tibetan crust? *Geology*. 27 (10), 943–946. [https://doi.org/10.1130/0091-7613\(1999\)027<0943:TSMLEF>2.3.CO;2](https://doi.org/10.1130/0091-7613(1999)027<0943:TSMLEF>2.3.CO;2).
- Armijo, R., Tapponier, P., Han, T.L., 1989. Late Cenozoic right-lateral strike-slip faulting in southern Tibet. *J. Geophys. Res. Solid Earth* 94, 2787–2838. <https://doi.org/10.1029/JB094iB03p02787>.
- Armijo, R., Tapponier, P., Mercier, J.L., Han, T.L., 1986. Quaternary extension in southern Tibet: Field observations and tectonic implications. *J. Geophys. Res.* 91 (B14), 13803–13872. <https://doi.org/10.1029/JB091iB14p13803>.
- Arnórsson, S., 1995. Geothermal systems in Iceland: structure and conceptual models-I. high temperature areas. *Geothermics* 24, 561–602.
- Arnórsson, S., 2000. Isotopic and chemical techniques in geothermal exploration, development and use. International Atomic Energy Agency, Vienna.
- Arnórsson, S., Andrsdóttir, A., 1995. Processes controlling the distribution of boron and chlorine in natural waters in Iceland. *Geochim. Cosmochim. Acta*. 59 (20), 4125–4126. [https://doi.org/10.1016/0016-7037\(95\)00278-8](https://doi.org/10.1016/0016-7037(95)00278-8).
- Bernard, R., Taran, Y., Pennisi, M., Tello, E., Ramirez, A., 2011. Chloride and Boron behavior in fluids of Los Humeros geothermal field (Mexico): A model based on the existence of deep acid brine. *Appl. Geochem.* 26 (12), 2064–2073. <https://doi.org/10.1016/j.apgeochem.2011.07.004>.
- Bertani, R., 2016. Geothermal power generation in the world 2010–2014 update report. *Geothermics*. 60, 31–43. <https://doi.org/10.1016/j.geothermics.2015.11.003>.
- Brown, L.D., Zhao, W.J., Nelson, K.D., Hauck, M., Alsdorf, D., Ross, A., Cogan, M., Clark, M., Liu, X.W., Che, J.K., 1996. Bright Spots, Structure, and Magmatism in Southern Tibet from INDEPTH Seismic Reflection Profiling. *Science*. 274.
- Burchfiel, B. C., Chen, Z.L., Hodges, K. V., Liu, Y.P., Royden, L. H., Deng, C.G., Xu, J.N., 1992. The South Tibetan Detachment System, Himalayan Orogen: Extension Contemporaneous With and Parallel to Shortening in a Collisional Mountain Belt: GSA Special Paper 269.
- Burg, J.P., Chen, G.M., 1984. Tectonics and structural zonation of southern Tibet. *China. Nature* 311 (20), 219–223.
- Chao, H.C., Pi, J.L., You, C.F., Shieh, Y.T., Lu, H.Y., Huang, K.F., Liu, H.C., Chung, C.H., 2021. Hydrogeology constrained by multi-isotopes and volatiles geochemistry of hot springs in Tatun Volcanic Group. *Taiwan. J. Hydrol.* 600, 126515 <https://doi.org/10.1016/j.jhydrol.2021.126515>.
- Chen, L.S., Booker, J.R., Jones, A.G., Wu, N., Unsworth, M.J., Wei, W.B., Tan, H.D., 1996. Electrically Conductive Crust in Southern Tibet from INDEPTH Magnetotelluric Surveying. *Science*. 274(5293), 1694–1696.
- Chen, Z., Liu, Y., Hodges, K.V., Burchfiel, B.C., Royden, L.H., Deng, C., 1990. The Kangmar Dome: A Metamorphic Core Complex in Southern Xizang (Tibet). *Science* 250, 1552–1556. <https://doi.org/10.1126/science.250.4987.1552>.
- Chiodini, G., Frondini, F., Cardellini, C., Peruzzi, L., 2000. Rate of diffuse carbon dioxide earth degassing estimated from carbon balance of regional aquifers: The case of central Apennine. *Italy. J. Geophys. Res.* 105, 8423–8434. <https://doi.org/10.1029/1999JB900355>.
- Chiodini, G., Cardellini, C., Amato, A., Boschi, E., Caliro, S., Frondini, F., Ventura, G., 2004. Carbon dioxide Earth degassing and seismogenesis in central and southern Italy. *Geophys. Res. Lett.* 31 (7), L07615. <https://doi.org/10.1029/2004gl019480>.
- Chiodini, G., Cardellini, C., Luccion, F.D., Selva, J., Frondini, F., Caliro, S., Rosiello, A., Bedini, G., Ventura, G., 2020. Correlation between tectonic CO<sub>2</sub> Earth degassing and seismicity is revealed by a 10-year record in the Apennines. *Italy. Sci. Adv.* 6 (35), eabc2938. <https://doi.org/10.1126/sciadv.abc2938>.
- Chung, S.L., Chu, M.F., Zhang, Y., Xie, Y., Lo, C.H., Lee, T.Y., Lan, C.Y., Li, X.H., Zhang, Q., Wang, Y.Z., 2005. Tibetan tectonic evolution inferred from spatial and temporal variations in post-collisional magmatism. *Earth-Sci. Rev.* 68 (3–4), 173–196. <https://doi.org/10.1016/j.earscirev.2004.05.001>.
- Clark, I., Fritz, P., 1997. *Environmental Isotopes in Hydrogeology*. Lewis Publishers, New York.
- Cogan, M.J., Nelson, K.D., Kidd, W.S.F., Wu, C., 1998. Shallow structure of the Yadong-Gulu rift, southern Tibet, from refraction analysis of Project INDEPTH common midpoint data. *Tectonics*. 17 (1), 46–61. <https://doi.org/10.1029/97tc03025>.
- Craig, H., 1963. The isotopic geochemistry of water and carbon in geothermal areas. In: Tongiorgi, E. (Ed.), *Nuclear Geology on Geothermal Areas*. Spoleto, Italy.
- Craig, H., 1961. Isotopic variations in meteor waters. *Science*. 133, 1702–1703. <https://doi.org/10.1126/science.133.3465.1702>.
- Delalande, M., Bergonzini, L., Gherardi, F., Guidi, M., Andre, L., Abdallah, I., Williamson, D., 2011. Fluid geochemistry of natural manifestations from the Southern Poroto-Rungwe hydrothermal system (Tanzania): Preliminary conceptual model. *J. Volcanol. Geotherm. Res.* 199 (1–2), 127–141. <https://doi.org/10.1016/j.jvolgeores.2010.11.002>.
- Dor, J., 2003. The basic characteristics of the Yangbajing geothermal field—a typical high temperature geothermal system. *Eng. Sci. 5* (1), 42–47 in Chinese with English abstract.
- Dotsika, E., 2012. Isotope and hydrochemical assessment of the Samothraki Island geothermal area, Greece. *J. Volcanol. Geotherm. Res.* 233–234, 18–26. <https://doi.org/10.1016/j.jvolgeores.2012.04.017>.
- Dotsika, E., 2015. H-O-C-S isotope and geochemical assessment of the geothermal area of Central Greece. *J. Geochem. Explor.* 150, 1–15. <https://doi.org/10.1016/j.jgexplo.2014.11.008>.
- Dupalova, T., Sracek, O., Vencelides, Z., Zak, K., 2012. The origin of thermal waters in the northeastern part of the Eger Rift, Czech Republic. *Appl. Geochem.* 27 (3), 689–702. <https://doi.org/10.1016/j.apgeochem.2011.11.016>.
- Fan, Y.F., Pang, Z.H., Liao, D.W., Tian, J., Hao, Y.L., Huang, T.M., Li, Y.M., 2019. Hydrogeochemical characteristics and genesis of geothermal water from the Ganzi geothermal field, eastern Tibetan Plateau. *Water* 11 (8), 1631. <https://doi.org/10.3390/w11081631>.
- Fan, J.J., Wang, Q., Li, J., Wei, G.J., Ma, J.L., Ma, L., Li, Q.W., Jiang, Z.Q., Zhang, L., Wang, Z.L., Zhang, L., 2021. Boron and molybdenum isotopic fractionation during crustal anatexis: Constraints from the Conadong leucogranites in the Himalayan Block, South Tibet. *Geochem. Cosmochim. Acta*. 297, 120–142. <https://doi.org/10.1016/j.gca.2021.01.005>.
- Fontes, J.C., Matray, J.M., 1993. Geochemistry and origin of formation brines from the Paris Basin, France: I. Brines associated with Triassic salts. *Chem. Geol.* 109, 149–175. [https://doi.org/10.1016/0009-2541\(93\)90068-T](https://doi.org/10.1016/0009-2541(93)90068-T).
- Fournier, R.O., 1977. Chemical geothermometers and mixing models for geothermal systems. *Geothermics*. 5 (1–4), 41–50. [https://doi.org/10.1016/0375-6505\(77\)90074-4](https://doi.org/10.1016/0375-6505(77)90074-4).
- Fournier, R.O., 1979. Geochemical and hydrologic considerations and the use of enthalpy-chloride diagrams in the prediction of underground conditions in hot-spring systems. *J. Volcanol. Geotherm. Res.* 5, 1–16. [https://doi.org/10.1016/0377-0273\(79\)90029-5](https://doi.org/10.1016/0377-0273(79)90029-5).
- Fournier, R.O., Truesdell, A.H., 1973. An empirical Na-K-Ca geothermometer for natural waters. *Geochem. Cosmochim. Acta*. 37, 1255–1275. [https://doi.org/10.1016/0016-7037\(73\)90060-4](https://doi.org/10.1016/0016-7037(73)90060-4).
- Freeze, R.A., Cherry, J.A., 1979. *Groundwater*. Prentice Hall, Englewood Cliffs, New Jersey.
- Frondini, F., Caliro, S., Cardellini, C., Chiodini, G., Morgantini, N., 2009. Carbon dioxide degassing and thermal energy release in the Monte Amiata volcanic-geothermal area (Italy). *Appl. Geochem.* 24 (5), 860–875. <https://doi.org/10.1016/j.apgeochem.2009.01.010>.
- Giggenbach, W.F., 1988. Geothermal solute equilibria. Derivation of Na-K-Mg-Ca geoindicators. *Geochim. Cosmochim. Acta*. 52 (12), 2749–2765. [https://doi.org/10.1016/0016-7037\(88\)90143-3](https://doi.org/10.1016/0016-7037(88)90143-3).
- Giggenbach, W.F., 1992. Isotopic shifts in waters from geothermal and volcanic systems along convergent plate boundaries and their origin. *Earth Planet. Sci. Lett.* 113, 495–510. [https://doi.org/10.1016/0012-821X\(92\)90127-H](https://doi.org/10.1016/0012-821X(92)90127-H).
- Giggenbach, W.F., 1995. Variations in the chemical and isotopic composition of fluids discharged over the Taupo Volcanic Zone. *J. Volcanol. Geotherm. Res.* 68, 89–116.
- Giggenbach, W.F., Soto, R.C., 1992. Isotopic and chemical composition of water and steam discharges from volcanic-magmatic-hydrothermal systems of the Guanacaste Geothermal Province, Costa Rica. *Appl. Geochem.* 7, 309–332. [https://doi.org/10.1016/0883-2927\(92\)90022-U](https://doi.org/10.1016/0883-2927(92)90022-U).
- Giggenbach, W.F., Sheppard, D.S., Robinson, B.W., Stewart, M.K., Lyon, G.L., 1994. Geothermal structure and position of the Waiautapu geothermal field, New Zealand. *Geothermics*. 23, 299–644.
- Goguel, R., 1983. The rare alkalies in hydrothermal alteration at Wairakei and Broadlands, geothermal fields, N.Z. *Geochem. Cosmochim. Acta*. 47, 429–437.
- Graven, H., Allison, C.E., Etheridge, D.M., Hammer, S., Keeling, R.F., Levin, I., Meijer, H. A.J., Rubino, M., Tans, P.P., Trudinger, C.M., Vaughn, B.H., White, J.W.C., 2017. Compiled records of carbon isotopes in atmospheric CO<sub>2</sub> for historical simulations in CMIP6. *Geosci. Model Dev.* 10, 4405–4417. <https://doi.org/10.5194/gmd-10-4405-2017>.
- Grimaud, D., Huang, S., Michard, G., Zheng, K., 1985. Chemical study of geothermal waters of central Tibet (China). *Geothermics* 14, 35–48.
- Guler, C., Thyne, G.D., 2004. Hydrologic and geologic factors controlling surface and groundwater chemistry in Indian Wells-Owens Valley area, southeastern California, USA. *J. Hydrol.* 285 (1–4), 177–198. <https://doi.org/10.1016/j.jhydrol.2003.08.019>.
- Guo, Q.H., 2012. Hydrogeochemistry of high-temperature geothermal systems in China: A review. *Appl. Geochem.* 27 (10), 1887–1898. <https://doi.org/10.1016/j.apgeochem.2012.07.006>.

- Guo, X., Gao, R., Zhao, J., Xu, X., Lu, Z., Klemperer, S.L., Liu, H., 2018. Deep-seated lithospheric geometry in revealing collapse of the Tibetan Plateau. *Earth Sci. Rev.* 185, 751–762. <https://doi.org/10.1016/j.earscirev.2018.07.013>.
- Guo, Q., Wang, Y., Liu, W., 2007. Major hydrogeochemical processes in the two reservoirs of the Yangbajing geothermal field, Tibet. *China. J. Volcanol. Geotherm. Res.* 166 (3–4), 255–268. <https://doi.org/10.1016/j.jvolgeores.2007.08.004>.
- Guo, Q., Wang, Y., Liu, W., 2009. Hydrogeochemistry and environmental impact of geothermal waters from Yangtze of Tibet. *China. J. Volcanol. Geotherm. Res.* 180 (1), 9–20. <https://doi.org/10.1016/j.jvolgeores.2008.11.034>.
- Guo, Q., Wang, Y., Liu, W., 2010. O, H, and Sr isotope evidences of mixing processes in two geothermal fluid reservoirs at Yangbajing, Tibet. *China. Environ. Earth Sci.* 59 (7), 1589–1597. <https://doi.org/10.1007/s12665-009-0145-y>.
- Guo, Q., Pang, Z.H., Wang, Y.C., Tian, J., 2017. Fluid geochemistry and geothermometry applications of the Kangding high-temperature geothermal system in eastern Himalayas. *Appl. Geochim.* 81, 63–75. <https://doi.org/10.1016/j.apgeochem.2017.03.007>.
- Guo, Q., Planer-Friedrich, B., Liu, M., Yan, K., Wu, G., 2019. Magmatic fluid input explaining the geochemical anomaly of very high arsenic in some southern Tibetan geothermal waters. *Chem. Geol.* 513, 32–43. <https://doi.org/10.1016/j.chemgeo.2019.03.008>.
- Hauk, M.L., Nelson, K.D., Brown, L.D., Zhao, W.J., Ross, A.R., 1998. Crustal structure of the Himalayan orogen at ~90° east longitude from Project INDEPTH deep reflection profiles. *Tectonics.* 17 (4), 481–500. <https://doi.org/10.1029/98tc01314>.
- He, L.F., Chen, L., Dor, J., Xi, X.L., Zhao, X.F., Chen, R.J., Yao, H.C., 2016. Mapping the Geothermal System Using AMT and MT in the Mapamyun (QP) Field. Lake Manasarovar, Southwestern Tibet. *Energies* 9 (10), 855. <https://doi.org/10.3390/en9100855>.
- Hensen, C., Nuzzo, M., Hornbrook, E., Pinheiro, L.M., Bock, B., Magalhaes, V.H., Brückmann, W., 2007a. Sources of mud volcano fluids in the Gulf of Cadiz—indications for hydrothermal imprint. *Geochim. Cosmochim. Acta.* 71 (5), 1232–1248. <https://doi.org/10.1016/j.gca.2006.11.022>.
- Hensen, C., Nuzzo, M., Hornbrook, E., Pinheiro, L.M., Bock, B., Magalhaes, V.H., Brückmann, W., 2007b. Sources of mud volcano fluids in the Gulf of Cadiz—indications for hydrothermal imprint. *Geochim. Cosmochim. Acta.* 71 (5), 1232–1248. <https://doi.org/10.1016/j.gca.2006.11.022>.
- Hasono, T., Yamamoto, C., 2021. Origins and pathways of deeply derived carbon and fluids observed in hot spring waters from non-active volcanic fields, western Kumamoto, Japan. *Earth, Planets and Space* 73 (1). <https://doi.org/10.1186/s40623-021-01478-1>.
- Hou, Z.Q., Duan, L.F., Lu, Y.J., Zheng, Y.C., Zhu, D.C., Yang, Z.M., Yang, Z.S., Wang, B. D., Pei, Y.R., Zhao, Z.D., McCuaig, T.C., 2015. Lithospheric architecture of the Lhasa Terrane and its control on ore deposits in the Himalayan-Tibetan Orogen. *Econ. Geol.* 110, 1541–1575. <https://doi.org/10.2113/econgeo.110.6.1541>.
- Hou, Z.Q., Li, Z.Q., Qu, X.M., Gao, Y.F., Hua, L.C., Zheng, M.P., Li, S.R., Yuan, W.M., 2001. The uplifting Processes of the Tibet Plateau since 0.5Ma B.P.: Evidences from Hydrothermal Activity in the Gangdise Belt. *Sci. China. Ser. D: Earth Sci.* 44, 35–44.
- Hou, Z.Q., Zheng, Y.C., Zeng, L.S., Gao, L.E., Huang, K.X., Li, W., Li, Q.Y., Fu, Q., Liang, W., Sun, Q.Z., 2012. Eocene-Oligocene granitoids in southern Tibet: Constraints on crustal anatexis and tectonic evolution of the Himalayan orogen. *Earth Planet. Sci. Lett.* 349–350, 38–52. <https://doi.org/10.1016/j.epsl.2012.06.030>.
- Hu, X.M., Wang, C.S., Li, X.H., 2001. The stable carbon isotope of Cretaceous carbonate and its response to paleo-ocean dissolved oxygen events in Southern Tibet. *Pro. Nat. Sci.* 10 (7), 341–349.
- Huang, Y., Zhao, Z.D., Zhang, F.Q., Zhu, D.C., Dong, G.C., Mo, X.X., 2010. Geochemistry and implication of the Gangdese batholiths from Renbu and Lhasa areas in southern Gangdese, Tibet. *Acta Petrol. Sin.* 26 (10), 3131–3142.
- Jankowski, J., Acworth, R.J., Shekarforoush, S., 1998. Reverse ion exchange in deeply weathered porphyritic dacite fractured aquifer system, Yass, New South Wales, Australia. In: Arehart, G.B., Hulston, J.R. (Eds.), Ninth Internat. Symp. Water - rock Interaction. A.A. Balkema, Rotterdam.
- Jiang, G.Z., Gao, P., Rao, S., Zhang, L.Y., Tang, X.Y., Huang, F., Zhao, P., Pang, Z.H., He, L.J., Hu, S.B., Wang, J.Y., 2016. Compilation of heat flow data in the continental area of China. *Geophys. J.* 59 (8), 2892–2910 (in Chinese). <http://doi.org/10.6038/cjg20160815>.
- Jolie, E., Scott, S., Faulds, J., Chambeffort, I., Axelsson, G., Gutiérrez-Negrín, L.C., Zemedkun, M.T., 2021. Geological controls on geothermal resources for power generation. *Nat. Rev. Earth Environ.* 2 (5), 324–339. <https://doi.org/10.1038/s43017-021-00154-y>.
- Kaasalainen, H., Stefansson, A., 2012. The chemistry of trace elements in surface geothermal waters and steam. *Iceland. Chem. Geol.* 330–331, 60–85. <https://doi.org/10.1016/j.chemgeo.2012.08.019>.
- Kapp, J.L.D.A., Harrison, T.M., Kapp, P., Grove, M., Lovera, O.M., Lin, D., 2005. Nyainqntanglha Shan: A window into the tectonic, thermal, and geochemical evolution of the Lhasa block, southern Tibet. *J. Geophys. Res.* 110 (B8) <https://doi.org/10.1029/2004jb003330>.
- Karlstrom, K.E., Crossey, L.J., Hilton, D.R., Barry, P.H., 2013. Mantle  $^3\text{He}$  and  $\text{CO}_2$  degassing in carbonic and geothermal springs of Colorado and implications for neotectonics of the Rocky Mountains. *Geology.* 41(4), 495–498. <https://doi.org/10.1130/G34007.1>.
- Karakus, H., Erguler, Z.A., Ozkul, C., Yanik, G., Kibici, Y., 2019. Geochemical and isotopic characteristics of geothermal discharges in the Emet Basin, Western Anatolia, Turkey. *Appl. Geochim.* 107, 105–119. <http://doi:10.1016/j.apgeochem.2019.06.002>.
- Kharaka, Y.K., Mariner, R.H., 1989. Chemical geothermometers and their application to formation waters from sedimentary basins. In: Naeser, N.D., McCulloch, T.H. (Eds.), *Thermal History of Sedimentary Basins: Methods and Case Histories*. SpringerVerlag, New York.
- Kidd, W.S.F., Pan, Y., Chang, C., Coward, M.P., Dewey, J.F., Gansser, A., Molnar, P., Shackleton, R.M., Sun, Y., 1988. Geological mapping of the Chinese-British Tibetan (Xizang-Qinghai) Plateau Geotraverse route. *Philos. Trans. R. Soc. London, Ser. A.* 327, 287–305.
- King, R., Ni, J., Zhao, W.J., Wu, J.X., Yuan, X.H., Zhao, L.S., Sandvol, E., Reese, C., Nabelek, J., Hearn, T., 1996. Evidence from earthquake data for a partially molten crustal layer in southern Tibet. *Science.* 274, 1692–1694.
- Kis, B.M., Baciu, C., Zsigmond, A.R., KekedyNagy, L., Karman, K., Palcsu, L., Mathe, I., Harangi, S., 2020. Constraints on the hydrogeochemistry and origin of the  $\text{CO}_2$ -rich mineral waters from the Eastern Carpathians – Transylvanian Basin boundary (Romania). *J. Hydrol.* 591 <https://doi.org/10.1016/j.jhydrol.2020.125311>.
- Klemperer, S.L., Zhao, P., Whyte, C.J., Darrah, T.H., Crossey, L.J., Karlstrom, K.E., Liu, T. Z., Winn, C., Hilton, D.R., Ding, L., 2022. Limited underthrusting of India below Tibet:  $^3\text{He}/^4\text{He}$  analysis of thermal springs locates the mantle suture in continental collision. *Proc. Natl. Acad. Sci. U. S. A.* 119 (12), e2113877119 <https://doi.org/10.1073/pnas.2113877119>.
- Kong, Y., Pang, Z., Shao, H., Hu, S., Kolditz, O., 2014. Recent studies on hydrothermal systems in China: a review. *Geotherm. Energy* 2, 19.
- Lambakis, N., Zagana, E., Katsanou, K., 2013. Geochemical patterns and origin of alkaline thermal waters in Central Greece (Platystomo and Smokovo areas). *Envir. Earth Sci.* 69 (8), 2475–2486. <https://doi.org/10.1007/s12665-012-2073-5>.
- Lee, J.M., Koh, D.C., Chae, G.T., Kee, W.S., Ko, K.-S., 2021. Integrated assessment of major element geochemistry and geological setting of traditional natural mineral water sources in South Korea at the national scale. *J. Hydrol.* 598, 126249 <https://doi.org/10.1016/j.jhydrol.2021.126249>.
- Li, X., Qi, J.H., Yi, L., Xu, M., Zhang, X.Y., Zhang, Q., Tang, Y.G., 2021. Hydrochemical characteristics and evolution of geothermal waters in the eastern Himalayan syntaxis geothermal field, southern Tibet. *Geothermics.* 97, 102233 <https://doi.org/10.1016/j.geothermics.2021.102233>.
- Li, Y.L., Wang, C.S., Dai, J.G., Xu, G.Q., Hou, Y.L., Li, X.H., 2015. Propagation of the deformation and growth of the Tibetan-Himalayan orogen: A review. *Earth Sci. Rev.* 143, 36–61. <https://doi.org/10.1016/j.earscirev.2015.01.001>.
- Li, X.H., Wang, C.S., Jenkyns, H.C., Cheng, X.R., Cui, J., Hu, X.M., 2005a. Bulk carbon isotope excursions of the Cenomanian through Turonian of mid Cretaceous in Southern Tibet. *Earth Sci.* 30 (3).
- Liao, Z., Zhao, P., 1999. Yunnan-Tibet Geothermal Belt-Geothermal Resources and Case Histories. Science Press, Beijing (in Chinese with English abstract).
- Liu, W., Guan, L.F., Liu, Y., Xie, X.G., Zhang, M.L., Chen, B.Y., Xu, S., Sano, Y.J., 2022. Fluid geochemistry and geothermal anomaly along the Yushu-Ganzi-Xianshuhe fault system, eastern Tibetan Plateau: Implications for regional seismic activity. *J. Hydrol.* 307, 127554.
- Liu, Z., Liu, W.J., Zhang, M., Xie, E.J., Liu, Z.M., Wang, G.L., 2014. Geothermal fluid genesis and mantle fluids contributions in Nimu-Naqu. *Tibet. Earth Sci. Front.* 21, 356–371.
- Lund, J.W., Toth, A.N., 2021. Direct utilization of geothermal energy 2020 worldwide review. *Geothermics.* 90, 101915 <https://doi.org/10.1016/j.geothermics.2020.101915>.
- Makovskiy, Y., Klemperer, S.L., Ratschbacher, L., Brown, L.D., Li, M., Zhao, W.J., Meng, F.L., 2019. INDEPTH wide-angle reflection observation of P-wave-to-S-wave conversion from crustal Bright Spots in Tibet. *Science.* 274, 1690–1691.
- Mao, X.M., Zhu, D.B., Ndikubwimanana, I., He, Y.Y., Shi, Z.D., 2021. The mechanism of high-salinity thermal groundwater in Xinzhou geothermal field, South China: Insight from water chemistry and stable isotopes. *J. Hydrol.* 593, 125889 <https://doi.org/10.1016/j.jhydrol.2020.125889>.
- Negri, A., Daniele, L., Aravena, D., Munoz, M., Delgado, A., Morata, D., 2018. Decoding fjord water contribution and geochemical processes in the Ayens thermal springs (Southern Patagonia, Chile). *J. Geochem. Explor.* 185, 1–13. <https://doi.org/10.1016/j.jgxpol.2017.10.026>.
- Nelson, K.D., Zhao, W.J., Brown, L.D., Kuo, J., Che, J.K., Liu, X.W., Klemperer, S.L., Makovskiy, Y., Meissner, R., Mechie, J., Kind, R., Wenzel, F., Nabelek, J., Chen, L.S., Tan, H.D., Wei, W.B., Jones, A.G., Booker, J., Unsworth, M., Kidd, W.S.F., Hauck, M., Alsdorf, D., Ross, A., Cogan, M., Wu, C.D., Sandvol, E., Edwards, M., 1996. Partially Molten Middle Crust Beneath Southern Tibet: Synthesis of Project INDEPTH Results. *Science.* 274, 1684–1687.
- Ni, H., Zhang, L., Xiong, X., Mao, Z., Wang, J., 2017. Supercritical fluids at subduction zones: evidence, formation condition, and physicochemical properties. *Earth Sci. Rev.* 167, 62–71.
- Nicholson, K., 1993. In: *Geothermal Fluids*. Springer, Berlin Heidelberg, Berlin, Heidelberg.
- Palandri, J.L., Reed, M.H., 2001. Reconstruction of in situ composition of sedimentary formation waters. *Geochim. Cosmochim. Acta.* 62, 1741–1767.
- Pan, G.T., Ding, J., Yao, D.S., 2004. Manual of the Tibetan Plateau and Its Adjacent Area Geological Map (1:1500000). Chengdu map publishing house (in Chinese).
- Pang, Z.H., Reed, M., 1998. Theoretical chemical thermometry on geothermal waters: Problems and methods. *Geochim. Cosmochim. Acta.* 62, 1083–1091.
- Parkhurst, D.L., Appelo, C.A.J., 2013. Description of Input and Examples for PHREEQC Version 3. A Computer Program for Speciation, Batch Reaction, One Dimensional Transport, and Inverse Geochemical Calculations, in: U.S. Geological Survey (Ed.), Techniques and Methods, Book 6, Chap. A43. U.S. Geological Survey, Denver, Colorado.
- Pasvanoglu, S.Z., 2020. Geochemistry and conceptual model of thermal waters from Ercīs – Zilan Valley. Eastern Turkey. *Geothermics.* 86, 101803 <https://doi.org/10.1016/j.geothermics.2020.101803>.

- Piper, M., 1944. A graphic procedure in the geochemical interpretation of wateranalyses. *Eos, Transactions American Geophysical Union* 25 (6), 914–928. <https://doi.org/10.1029/TR025i006p00914>.
- Qiu, X., Wang, Y., Wang, Z., Regenauer-Lieb, K., Zhang, K., Liu, J., 2018. Determining the origin, circulation path and residence time of geothermal groundwater using multiple isotopic techniques in the Heyuan Fault Zone of Southern China. *J. Hydrol.* 567, 339–350. <https://doi.org/10.1016/j.jhydrol.2018.10.010>.
- Raychowdhury, N., Mukherjee, A., Bhattacharya, P., Johannesson, K., Bundschuh, J., Sifuentes, G.B., Nordberg, E., Martin, R.A., Storniolo, A.D.R.S., 2014. Provenance and fate of arsenic and other solutes in the Chaco-Pampean Plain of the Andean foreland, Argentina: From perspectives of hydrogeochemical modeling and regional tectonic setting. *J. Hydrol.* 518, 300–316. <https://doi.org/10.1016/j.jhydrol.2013.07.003>.
- Reed, M., Spycher, N., 1984. Calculation of pH and mineral equilibria in hydrothermal waters with application to geothermometry and studies of boiling and dilution. *Geochim. Cosmochim. Acta* 48, 1479–1492.
- Reed, M., Spycher, N., Palandri, J., 2012. SOLVEQ-XPT: a Computer Program for Computing Aqueous-mineral-gas Equilibria. Department of Geological Sciences, University of Oregon, Eugene, OR.
- Reyes, A.G., Trompette, W.J., 2012. Hydrothermal water-rock interaction and the redistribution of Li, B and Cl in the Taupo Volcanic Zone, New Zealand. *Chem. Geol.* 314, 96–112. <https://doi.org/10.1016/j.chemgeo.2012.05.002>.
- Rezaei, A., Rezaeian, M., Porkhial, S., 2019. The hydrogeochemistry and geothermometry of the thermal waters in the Mouli Graben, Sabalan volcano, NW Iran. *Geothermics*. 78, 9–27. <https://doi.org/10.1016/j.geothermics.2018.11.006>.
- Searle, M.P., Windley, B.F., Coward, M.P., Cooper, D.J.W., Rex, A.J., Rex, D., Li, T.D., Xiao, X.C., Jan, M.Q., Thakur, V.C., Kumar, 1987. The closing of Tethys and the tectonics of the Himalaya. *Geol. Soc. Am. Bull.* 98, 378–701.
- Shoedarto, R.M., Tada, Y., Kashiwaya, K., Koike, K., Iskandar, I., 2020. Specifying recharge zones and mechanisms of the transitional geothermal field through hydrogen and oxygen isotope analyses with consideration of water-rock interaction. *Geothermics*. 86, 101797 <https://doi.org/10.1016/j.geothermics.2019.101797>.
- Slacek, O., Hirata, R., 2002. Geochemical and stable isotopic evolution of the Guarani Aquifer System in the state of São Paulo, Brazil. *Hydrogeol. J.* 10 (6), 643–655. <https://doi.org/10.1007/s10040-002-0222-8>.
- Slacek, O., Rahobisoa, J.J., Trubac, J., Buzek, F., Andriamananjy, S.A., Rambeloson, R. A., 2019. Geochemistry of thermal waters and arsenic enrichment at Antsirabe. Central Highlands of Madagascar. *J. Hydrol.* 577, 123895 <https://doi.org/10.1016/j.jhydrol.2019.06.067>.
- Tan, H.B., Zhang, Y.F., Zhang, W.J., Kong, N., Zhang, Q., Huang, J.Z., 2014. Understanding the circulation of geothermal waters in the Tibetan Plateau using oxygen and hydrogen stable isotopes. *Appl. Geochem.* 51, 23–32. <https://doi.org/10.1016/j.apgeochem.2014.09.006>.
- Taylor, M., Yin, A., 2009. Active structures of the Himalayan-Tibetan orogen and their relationships to earthquake distribution, contemporary strain field, and Cenozoic volcanism. *Geosphere* 5 (3), 199–214. <https://doi.org/10.1130/ges00217.1>.
- Taylor, B. E., 1992. Degassing of H<sub>2</sub>O from rhyolite magma during eruption and shallow intrusion, and the isotopic composition of magmatic water in hydrothermal systems. In: *Magmatic Contributions to Geothermal Systems* (Edited by Hedenquist, J. W.), Report n. 279, pp. 190–194. Geological Survey of Japan, Tsukuba, Japan.
- Tong, W., Liao, Z.J., Liu, S.B., Zhang, Z.J., You, M.Z., Zhang, M.T., 2000. Thermal Springs in Tibet. Science Press, Beijing (in Chinese).
- Truesdell, A., Fournier, R., 1977. Procedure for estimating the temperature of a hotwater component in a mixed water by using a plot of dissolved silica versus enthalpy. *Journal of Research of the US Geological Survey* 5 (1), 49–52.
- Unsworth, M.J., Jones, A.G., Wei, W., Marquis, G., Gokarn, S.G., Spratt, J.E., Team, I.M., 2005. Crustal rheology of the Himalaya and Southern Tibet inferred from magnetotelluric data. *Nature* 438 (7064), 78–81. <https://doi.org/10.1038/nature04154>.
- Verma, S., Mukherjee, A., Mahanta, C., Choudhury, R., Mitra, K., 2016. Influence of geology on groundwater-sediment interactions in arsenic enriched tectono-morphic aquifers of the Himalayan Brahmaputra river basin. *J. Hydrol.* 540, 176–195. <https://doi.org/10.1016/j.jhydrol.2016.05.041>.
- Verma, S.P., Santoyo, E., 1997. New improved equations for Na/K, Na/Li and SiO<sub>2</sub> geothermometers by outlier detection and rejection. *J. Volcanol. Geoth. Res.* 79, 9–23. [https://doi.org/10.1016/S0377-0273\(97\)00024-3](https://doi.org/10.1016/S0377-0273(97)00024-3).
- Wang, X., Wang, G.L., Lu, C., GaO, H.N., Liu, Z., 2018a. Evolution of deep parent fluids of geothermal fields in the Nuru-Nagchu geothermal belt, Tibet, China. *Geothermics*. <https://doi.org/10.1016/j.geothermics.2017.07.010>.
- Wang, Y., Li, L., Wen, H., Hao, Y., 2022. Geochemical evidence for the nonexistence of supercritical geothermal fluids at the Yangbajing geothermal field, southern Tibet. *J. Hydrol.* 604, 127243 <https://doi.org/10.1016/j.jhydrol.2021.127243>.
- Wang, X., Wang, G.L., Gan, H.N., Liu, Z., Nan, D.W., 2018b. Hydrochemical Characteristics and Evolution of Geothermal Fluids in the Chabu High-Temperature Geothermal System, Southern Tibet. *Geofluids*. 2018, 1–15. <https://doi.org/10.1155/2018/8532840>.
- Wang, C.G., Zheng, M.P., Zhang, X.F., Qian, W., Liu, X.F., Ren, J.H., Chen, S.S., 2021. Geothermal-type Lithium Resources in Southern Xizang, China. *Acta Geol. Sin.* 95 <https://doi.org/10.1111/1755-6724.14675>.
- Wei, W., Unsworth, M., Jones, A., Booker, J., Tan, H.D., Nelson, D., Chen, L.S., Li, S.H., Solon, K., Bedrosian, P., Jin, S., Deng, M., Ledo, J.J., Kay, D., Roberts, B., 2001. Detection of Widespread Fluids in the Tibetan Crust by Magnetotelluric Studies. *Science* 292(5517), 716–719.
- Williams, A.J., Crossey, L.J., Karlstrom, K.E., Newell, D., Person, M., Woolsey, E., 2013. Hydrochemistry of the Middle Rio Grande aquifer system – Fluid mixing and salinization of the Rio Grande due to fault inputs. *Chem. Geol.* 351, 281–298. <https://doi.org/10.1016/j.chemgeo.2013.05.029>.
- Wrage, J., Tardani, D., Reich, M., Daniele, L., Arancibia, G., Cembrano, J., Sanchez-Alfar, P., Morata, D., Perez-Moreno, R., 2017. Geochemistry of thermal waters in the Southern Volcanic Zone, Chile - Implications for structural controls on geothermal fluid composition. *Chem. Geol.* 466, 545–561. <https://doi.org/10.1016/j.chemgeo.2017.07.004>.
- Wu, Z.H., Ye, P.S., Barosh, P.J., Wu, Z.H., 2011. The October 6, 2008 Mw 6.3 magnitude Damxung earthquake, Yadong-Gulu rift, Tibet, and implications for present-day crustal deformation within Tibet. *J. Asian Earth Sci.* 40, 943–957. <https://doi.org/10.1016/j.jseas.2010.05.003>.
- Wu, Z.H., Ye, P.S., Wang, C.M., Zhang, K.Q., Zhao, H., Zheng, Y.G., Yin, J.H., Li, H.H., 2015. The reliabilities, ages, significance of prehistoric large earthquakes in Angang graben in South Tibet. *Earth Science-Journal of China university of geosciences*. 40, 1621–1642.
- Wu, Y.Q., Zhou, X., Wang, M.M., Zhuo, L.Y., Xu, H.F., Liu, Y., 2021. Comparison of hydrogeological characteristics and genesis of the Xiaguan Hot Spring and the Butterfly Spring in Yunnan of China. *J. Hydrol.* 593, 125922 <https://doi.org/10.1016/j.jhydrol.2020.125922>.
- Xie, C.L., Jin, S., Wei, W.B., Ye, G.F., Jing, J.E., Zhang, L.T., Dong, H., Yin, Y.T., 2021. Middle Crustal Partial Melting Triggered Since the Mid-Miocene in Southern Tibet: Insights From Magnetotelluric Data. *J. Geophys. Res.* 126 <https://doi.org/10.1029/2021JB022435>.
- Yang, P., Cheng, Q., Xie, S., Wang, J., Chang, L., Yu, Q., Zhan, Z.J., Chen, F., 2017. Hydrogeochemistry and geothermometry of deep thermal water in the carbonate formation in the main urban area of Chongqing, China. *J. Hydrol.* 549, 50–61. <https://doi.org/10.1016/j.jhydrol.2017.03.054>.
- Yang, P., Luo, D., Hong, A.H., Ham, B., Xie, S.Y., Ming, X.X., Wang, Z.X., Pang, Z.H., 2019. Hydrogeochemistry and geothermometry of the carbonate-evaporite aquifers controlled by deep-seated faults using major ions and environmental isotopes. *J. Hydrol.* 579, 50–61. <https://doi.org/10.1016/j.jhydrol.2019.124116>.
- Yi, L., Qi, J., Li, X., Xu, M., Zhang, X., Zhang, Q., Tang, Y., 2021. Geochemical characteristics and genesis of the high-temperature geothermal systems in the north section of the Sanjiang Orogenic belt in southeast Tibetan Plateau. *J. Volcanol. Geother. Res.* 414 <https://doi.org/10.1016/j.jvolgeores.2021.107244>.
- Yin, A., Harrison, T.M., 2000. Geologic evolution of the Himalayan Tethyan orogen. *Annu. Rev. Earth Planet. Sci.* 28, 211–280. <https://doi.org/10.1146/annurev.earth.28.1.211>.
- Yu, J.S., Zhang, H.B., Yu, F.J., Liu, D.P., 1984. Oxygen and Hydrogen isotopic compositions of meteoric waters in the eastern part of xizang. *Geochemistry*. 3 (2), 93–101.
- Yuan, J.F., Guo, Q.H., Wang, Y.X., 2014. Geochemical behaviors of boron and its isotopes in aqueous environment of the Yangbajing and Yangyi geothermal fields, Tibet, China. *J. Geochem. Explor.* 140, 11–22. <https://doi.org/10.1016/j.gexplo.2014.01.006>.
- Zhang, L., Chen, S., Zhang, C., 2019b. Geothermal power generation in China: Status and prospects. *Energy Sci. Eng.* 7, 1428–1450.
- Zhang, M., Lin, W.J., Liu, Z., Liu, Z. M., Hu, X. C., Wang, G. L., 2014. Hydrogeochemical characteristics and genetic model of Gulu high-temperature geothermal system in Tibet, China. *Journal of Chengdu University of Technology(Science & Technology Edition)*, 41(3):382-392 (in Chinese with English abstract).
- Zhang, L.H., Guo, Z.F., Sano, Y., Zhang, M., Sun, Y., Cheng, Z., Yang, T.F., 2017. Flux and genesis of CO<sub>2</sub> degassing from volcanic-geothermal fields of Gulu-Yadong rift in the Lhasa terrane, South Tibet: Constraints on characteristics of deep carbon cycle in the India-Asia continent subduction zone. *J. Asian Earth Sci.* 149, 110–123. <https://doi.org/10.1016/j.jseas.2017.05.036>.
- Zhang, G., Lu, P., Zhang, Y., Tu, K., Zhu, C., 2020. SupPhreeqc: A program for generating customized Phreeqc thermodynamic datasets from Supertrtl and extending calculations to elevated pressures and temperatures. *Comput. Geosci.* 143, 104560.
- Zhang, W., Wang, G.L., Xing, L.X., Li, T.X., Zhao, J.Y., 2019a. Geochemical response of deep geothermal processes in the Litang region, Western Sichuan. *Energy Explor. Exploit.* 37, 626–645. <https://doi.org/10.1177/0144598718812550>.
- Zhang, M.L., Zhang, L.H., Zhao, W.B., Guo, Z.F., Xu, S., Sano, Y.J., Lang, Y.C., Liu, C.Q., Li, Y., 2021. Metamorphic CO<sub>2</sub> emissions from the southern Yadong-Gulu rift, Tibetan Plateau: Insights into deep carbon cycle in the India-Asia continental collision zone. *Chemi. Geol.* 584, 120534 <https://doi.org/10.1016/j.chemgeo.2021.120534>.
- Zhao, P., Jin, J., Zhang, H., Duo, J., Liang, T., 1998. Chemical composition of thermal water in the Yangbajing geothermal field, Tibet. *Sci. Geol. Sini.* 33(1), 61–72 in Chinese with English abstract.
- Zhu, M.X., Xu, Y., 1989. Hydrothermal alteration in the Yangbajain geothermal field. *Tibet. Chin. J. Geol.* 2, 162–173 in Chinese with English abstract.
- Zuo, J., Wu, Z., Ha, G., Hu, M., Zhou, C., Gai, H., 2021. Spatial variation of nearly NS-trending normal faulting in the southern Yadong-Gulu rift, Tibet: New constraints from the Chongba Yumtso fault, Duoqing Co graben. *J. Struct. Geol.* 144, 104256. <https://doi.org/10.1016/j.jsg.2020.104256>.

## Further reading

- Li, Z.Q., Hou, Z.Q., Nie, F.J., Meng, X.J., 2005b. Characteristic and Distribution of the Partial Melting Layers in the Upper Crust: Evidence from Active Hydrothermal Fluid in the South Tibet. *Acta Geol. Sin.* 79, 68–77.